

## DUST SEDS IN THE ERA OF HERSCHEL AND PLANCK: A HIERARCHICAL BAYESIAN FITTING TECHNIQUE

BRANDON C. KELLY<sup>1,2</sup>, RAHUL SHETTY<sup>3</sup>, AMELIA M. STUTZ<sup>4</sup>, JENS KAUFFMANN<sup>5</sup>, ALYSSA A. GOODMAN<sup>1</sup>, RALF LAUNHARDT<sup>4</sup>*Draft version February 7, 2022*

## ABSTRACT

We present a hierarchical Bayesian method for fitting infrared spectral energy distributions (SEDs) of dust emission to observed fluxes. Under the standard assumption of optically thin single temperature ( $T$ ) sources the dust SED as represented by a power-law modified black body is subject to a strong degeneracy between  $T$  and the spectral index  $\beta$ . The traditional non-hierarchical approaches, typically based on  $\chi^2$  minimization, are severely limited by this degeneracy, as it produces an artificial anti-correlation between  $T$  and  $\beta$  even with modest levels of observational noise. The hierarchical Bayesian method rigorously and self-consistently treats measurement uncertainties, including calibration and noise, resulting in more precise SED fits. As a result, the Bayesian fits do not produce any spurious anti-correlations between the SED parameters due to measurement uncertainty. We demonstrate that the Bayesian method is substantially more accurate than the  $\chi^2$  fit in recovering the SED parameters, as well as the correlations between them. As an illustration, we apply our method to *Herschel* and submillimeter ground-based observations of the star-forming Bok globule CB244. This source is a small, nearby molecular cloud containing a single low-mass protostar and a starless core. We find that  $T$  and  $\beta$  are weakly positively correlated – in contradiction with the  $\chi^2$  fits, which indicate a  $T - \beta$  anti-correlation from the same data-set. Additionally, in comparison to the  $\chi^2$  fits the Bayesian SED parameter estimates exhibit a reduced range in values.

*Subject headings:* infrared: ISM — ISM: dust — ISM: structure — methods: data analysis — methods: statistical — stars: formation

## 1. INTRODUCTION

Dust provides an important observational avenue for investigating a variety of astrophysical environments. Though dust amounts to only a fraction ( $\sim 1/100$ ) of the gaseous mass, it is an efficient radiator and thus provides clues to the energy content of the interstellar medium (ISM). Dust grains are heated by a variety of sources, such as stellar radiation or collisions with gas, and re-radiates most of this energy as thermal emission. For temperatures characteristic of the ISM, thermal emission from dust is predominantly at far infrared (IR) and sub-millimeter wavelengths. Consequently, properties of the far-IR and sub-mm spectral energy distribution (SED) can provide vital information about the physical state of observed systems. For example, the amount of emergent IR flux scales proportionally with the star formation rate in (ultra) luminous infrared galaxies ([U]LIRGs, e.g., Lagache et al. 2005); SED shapes indicate the evolutionary state of star forming cores within molecular clouds (e.g., Adams et al. 1987); and grain evolution in protoplanetary disks can be modeled using measured SEDs (e.g., Watson et al. 2007). Understanding dust SEDs therefore represents a crucial step in numerous research

fields spanning a wide range of spatial scales. Ground and space based telescopes, such as *IRAS*, *ISO*, *Spitzer*, *Herschel*, *Planck*, SCUBA(2), MAMBO(2), SABOCA, and new instruments on *SOFIA* have and continue to measure IR emission, with the aim of quantifying dust SEDs.

At far-IR wavelengths ( $\lambda \gtrsim 60 \mu\text{m}$ ) the shape of SEDs due to thermal emission from dust is empirically found to be well represented as a Planck function,  $B_\nu(T)$ , evaluated at the dust temperature  $T$ , modified by a power law in frequency,  $\nu^\beta$  (Hildebrand 1983):

$$S_\nu = \Omega N \kappa_0 \left( \frac{\nu}{\nu_0} \right)^\beta B_\nu(T). \quad (1)$$

Here,  $\Omega$  is the solid angle of the observing beam,  $N$  is the column density,  $B_\nu(T)$  is the Planck function, and  $\kappa_0(\nu/\nu_0)^\beta$  is the opacity of the emitting dust. Note that  $\tau_0 = N\kappa_0$  is the optical depth at frequency  $\nu_0$ . An essential assumption in Equation 1 is that dust is optically thin, so that  $\tau(\nu) \ll 1$ . Following convention, we assume that the opacity  $\kappa_0$  is known, and employ  $\kappa_0 = 0.009 \text{ cm}^2/\text{g}$  (Ossenkopf & Henning 1994), which accounts for the dust-to-gas ratio, so that the free parameter in the fit is the gas column density  $N$ . The spectral index  $\beta$  determines the opacity  $\kappa_\nu$  of the dust, and encodes information about grain composition. Usually,  $\beta$  is found to be  $\sim 2$  for silicate and/or carbonaceous grain composition common in the diffuse ISM (Draine & Lee 1984).

Numerous observational investigations have focused on measuring the value of  $\beta$ . Most observational analyses estimate  $T$  and  $\beta$  by employing a least-squares ( $\chi^2$ ) SED

<sup>1</sup> Harvard-Smithsonian Center for Astrophysics, 60 Garden Street, Cambridge, MA 02138

<sup>2</sup> Department of Physics, Broida Hall, University of California, Santa Barbara, CA 93106-9530

<sup>3</sup> Zentrum für Astronomie der Universität Heidelberg, Institut für Theoretische Astrophysik, Albert-Ueberle-Str. 2, 69120 Heidelberg, Germany

<sup>4</sup> Max Planck Institut für Astronomie, Königstuhl 17, 69117 Heidelberg, Germany

<sup>5</sup> NASA JPL, 4800 Oak Grove Drive, Pasadena, CA 91109

fit. However, due to the degeneracy between  $T$  and  $\beta$ , known since the earliest efforts to derive dust properties from a limited number of far-IR and submillimeter measurements (Keene et al. 1980),  $\chi^2$  fits underestimating  $\beta$  will naturally overestimate  $T$  (Blain et al. 2003; Sajina et al. 2006), or vice versa. Erroneous estimates of  $T$  and/or  $\beta$  may arise due to the inaccurate assumption of a constant temperature along the line-of-sight (Shetty et al. 2009b), or uncertainty in the flux measurements. Additionally, the presence of internal sources may also yield an artificial  $T - \beta$  anti-correlation in the estimated SED (Malinen et al. 2011). Shetty et al. (2009a) demonstrate through Monte Carlo simulations that modest noise levels can lead to spurious  $T - \beta$  anti-correlations. Employing models of isothermal sources with constant  $\beta$ , they show that due to uncertainties as low as 5%,  $\chi^2$  fits produce erroneous  $T$  and  $\beta$  estimates. Moreover, the fits result in an artificial  $T - \beta$  anti-correlation which is remarkably similar to the trend derived from observational investigations. Shetty et al. (2009a) conclude that  $\chi^2$  SED fits cannot reliably reveal the true  $T - \beta$  correlation under realistic conditions where noise is present.

This  $T - \beta$  degeneracy may have obscured the relationship between dust temperature and composition present in astrophysical sources. Observational investigations employing careful statistical analyses also conclude that the  $T - \beta$  anti-correlation derived from  $\chi^2$  fits may be spurious. Schnee et al. (2010) demonstrate that though a  $\chi^2$  fit to fluxes from the starless core TMC-1C produces the anti-correlation, due to the degeneracy between  $T$  and  $\beta$  the data is also consistent with a constant  $\beta$  throughout the source. Using radiative transfer modeling, Juvela et al. (2011) suggest that line-of-sight temperature variations may be responsible for the  $\chi^2$  estimate of a decrease in  $\beta$  towards an internally heated core.

Accurately measuring  $\beta$  and  $T$  is essential for understanding grain growth and evolution. Under the dust coagulation scenario, a higher frequency of dust agglomeration in dense regions results in increased grain sizes. In protoplanetary disks,  $\beta$  is usually measured to be  $\lesssim 1$  (e.g. Miyake & Nakagawa 1993; Mannings & Emerson 1994; Draine 2006), lower than the larger scale ISM value of  $\beta \sim 2$  (Draine & Lee 1984). Goldsmith et al. (1997) found some indications of a decrease in  $\beta$  towards higher density gas in the Orion molecular cloud. In broad terms, temperatures are generally lower in higher density regions (away from embedded sources) due to more effective shielding from the ambient interstellar radiation field. Thus, in the dust coagulation scenario the decrease in  $\beta$  towards denser regions should be associated with a decrease in temperature and an increase in density.

On the other hand,  $\chi^2$  SED fitting from various sources – from starless cores to entire galaxies – suggests that  $\beta$  increases with decreasing  $T$ . Using *IRAS* and balloon-borne *PRONAOS* observations of various sources, Dupac et al. (2003) found an inverse correlation between the spectral index and temperature, with  $\beta$  ranging from 0.8 to 2.4, and  $T$  ranging from 11 to 80 K. Dupac et al. (2003) suggested that the hyperbolic shape of the  $T - \beta$  anti-correlation may have a physical basis, such as a variation of dust composition with

temperature. Yang & Phillips (2007) found a similar trend from a sample of LIRGs, although Hayward et al. (2011) argue that the optically thin isothermal SED model is inappropriate for extra-galactic sources, at least for sub-mm galaxies. More recently, SEDs derived from *Herschel* and *Planck* observations have also conveyed  $T - \beta$  anti-correlations (e.g. Anderson et al. 2010; Paradis et al. 2010; Planck Collaboration et al. 2011). These results are interpreted to be in agreement with laboratory studies: laboratory measurements of some amorphous materials also show a  $T - \beta$  anti-correlation (e.g. Agladze et al. 1996; Boudet et al. 2005). However, those laboratory results depend on grain composition and wavelength, and do not consider how variations in (volume) densities similar to the range found in the ISM can affect the results. The comparison is further complicated by the spurious anti-correlation arising in  $\chi^2$  fits due to noise (Shetty et al. 2009a), and by variations of temperature and dust composition along the line-of-sight (Shetty et al. 2009b; Malinen et al. 2011; Juvela et al. 2011).

Properly treating the degeneracy between  $T$  and  $\beta$  is thus a necessity for accurately fitting dust SEDs and assessing any variation of grain properties with temperature. The motivation for this work stems from the  $T - \beta$  anti-correlation found in observational analysis which appear to be very similar to the spurious anti-correlation due solely to statistical uncertainties (Shetty et al. 2009a). The main goal of this work is to develop a SED fitting method that rigorously treats statistical uncertainties so that spurious  $T - \beta$  anti-correlations are avoided. To satisfy these conditions, we introduce a hierarchical Bayesian approach for fitting an ensemble of dust SEDs.

Hierarchical<sup>2</sup> modeling is a statistical framework that was developed to handle data analysis problems with multiple stages (e.g., Gelman & Hill 2007). Hierarchical models are preferred for complex data analysis problems, as they are able to effectively handle multiple sources of uncertainty at all stages of the data analysis. Sources of statistical uncertainties include random noise and calibration (correlated) errors, which can contribute both multiplicative and additive components. Hierarchical models can account for correlated uncertainties and degeneracies between parameters, and may thus avoid any spurious correlations. Moreover, Bayesian methods calculate the probability distribution of the parameters given the measured data, so that the uncertainties returned by the inference are rigorous and well-defined. This ensures that all sources of measurement error are properly incorporated into the uncertainties in the estimated parameters. This is in stark contrast to more traditional frequentist and approximate methods, such as the propagation of errors or the treatment of the best-fit values as the true values. Frequentist approaches can lead to biases and incorrect quantification of uncertainty in complex problems. Bayesian methods have been shown to avoid such biases for numerous problems in a variety of scientific disciplines, and, as we demonstrate in this work, can effectively handle the degeneracy between  $T$  and  $\beta$  in SED fitting.

This paper is organized as follows. In the next sec-

<sup>2</sup> Also called “multilevel” modeling.

tion, we describe our hierarchical Bayesian model, and contrast it with the  $\chi^2$  fit. In Section 3, we test the Bayesian method on model data, and compare the results to a  $\chi^2$  fit. We apply the Bayesian fit to observed fluxes from starforming core CB244 in Section 4. After a brief discussion on the interpretation of our results in Section 5, we provide a summary in Section 6.

## 2. THE HIERARCHICAL STATISTICAL MODEL

In this section, we present a hierarchical Bayesian technique that simultaneously estimates the values of the column density  $N$ , spectral index  $\beta$ , and temperature  $T$ , as well as their joint distribution, directly from a set of observed fluxes. Although hierarchical Bayesian modeling is becoming more common in astrophysics (e.g., Loredo 2004; Kelly 2007; Hogg et al. 2010; Mandel et al. 2011), it is not nearly as widely employed in most astrophysical fields as traditional single-level methods. In order to allow the reader to become familiar with the hierarchical modeling approach, we begin by providing an overview of the method in Section 2.1. To guide readers familiar with single-level frequentist methods, we also contrast it with the minimized- $\chi^2$  fit, which is commonly employed for estimating  $N$ ,  $\beta$ , and  $T$ . A thorough description of the particular hierarchical Bayesian model we develop is subsequently given in Sections 2.2 and 2.3. Gelman et al. (2004) provides a clear overview of Bayesian methods, including hierarchical models, and Carroll et al. (2006) is a good reference on methods for dealing with measurement errors; both references also discuss Markov Chain Monte Carlo (MCMC) methods.

The power of Bayesian analysis is reflected in its output, which for our problem is a probability distribution for each value of  $N$ ,  $\beta$ , and  $T$  for each pixel, as well as for the parameters defining the joint distribution of  $N$ ,  $\beta$ , and  $T$ , given the measured data.<sup>3</sup> The probability distribution of the parameters given the observed data is called the *posterior* distribution, and provides a complete and straight-forward description of our uncertainty in the parameters. This is contrasted with the output of the frequentist methods, such as  $\chi^2$  or maximum-likelihood estimates, as frequentist methods provide a point estimate of the parameters and sometimes an estimate of a confidence region. However, while Bayesian posteriors are exact, the frequentist analogues, i.e., confidence regions, are often difficult to estimate for complex problems, such as the one we are addressing.

### 2.1. Basics of Hierarchical Modeling of Dust SEDs

Traditionally, parameters for SED models have been estimated by minimizing  $\chi^2$ . More recently, non-hierarchical Bayesian methods have been used to estimate the parameters for individual pixels or sources (Paradis et al. 2010). These methods are appropriate if the goal is to estimate the SED parameters for a single pixel or source, as there is only one level to the data analysis problem: the measured flux values are generated from the SED parameters for an individual pixel or source. In this case, one only needs a measurement

model for the data, e.g., that the measured data are obtained by contaminating the SED at the observational wavelengths with Gaussian measurement noise. However, for most scientific problems of interest, the data analysis problem has multiple stages, for which traditional non-hierarchical methods, such as those based on  $\chi^2$ , are not applicable and lead to biases. Within the context of the problem that we are addressing, namely the distribution of parameters for dust SEDs, there are at least two levels to the data analysis problem. First, there is the level corresponding to how the SED parameters for individual pixels or sources are generated from the distribution of these parameters. Second, there is the level corresponding to how the measured fluxes are generated from the SED parameters for individual pixels or sources. The point of hierarchical modeling is to model and fit both levels simultaneously.

Under the traditional non-hierarchical approach, statistical inference at the first (distribution) level would be performed using the best-fit results from the second (individual SED) level; i.e., the distribution of the SED parameters is estimated directly from the best-fit values for individual pixels or sources obtained by minimizing  $\chi^2$ , effectively treating the best-fit values as if they were the true values. However, these best-fit values are estimated with error. The distribution of the estimates is the convolution of the distribution of the true values of the SED parameters with the error distribution of their estimates. Therefore, the distribution of the quantities estimated using non-hierarchical methods will always be a biased estimate of the distribution of the true values, or rather the distribution of the values that would have been obtained in the absence of measurement errors. Within the context of the  $\beta$ - $T$  relationship, this implies that the distribution of  $\beta$  and  $T$  estimated using the  $\chi^2$ -based estimates will always be biased toward an anti-correlation, as the error distribution of  $\beta$  and  $T$  is anti-correlated. This is a mathematical fact and is true for any value of the  $S/N$ , although distributions inferred from higher  $S/N$  data will not be as biased. The reason for this is because the traditional non-hierarchical methods do not effectively treat errors at all levels of the data analysis problem.

Within the context of estimating SED parameters and their distribution, a hierarchical model is constructed by invoking a model for the distribution of SED parameters, as well as a model for the measured data. The model for the distribution of SED parameters has its own set of free parameters, and all that is assumed is the functional form. For example, one could assume that the distribution of SED parameters is a Gaussian distribution, and then the free parameters would be the mean and covariance of the SED parameters. Both the model for the distribution of the SED parameters, and the SED parameters for individual pixels or sources, are fit simultaneously. This approach is able to effectively handle uncertainty at all levels of the data analysis problem, and thus does not suffer from the biases that traditional non-hierarchical approaches do when estimating the distribution of SED parameters. Moreover, because one assumes a model for the distribution of the SED parameters, and fits all of the pixels or sources simultaneously, one is able to obtain more precise estimates of the SED parameters for individual sources as all of the information is pooled

<sup>3</sup> Often in practice, Bayesian algorithms do not output the probability distribution of the parameters directly, but rather output a set of random draws of the parameters from their posterior probability distribution.

together.

The difference between the traditional and hierarchical modeling approaches may be more easily understood by using an analogy with astronomical imaging. As an example, consider the  $\beta$ - $T$  distribution. The distribution of the estimated values of  $\beta$  and  $T$  is the convolution of the distribution of the true values with their banana-shaped error distribution. Therefore, the error distribution of  $\beta$  and  $T$  can be thought of as a ‘PSF’ which acts on the image of the distribution of the true values of the parameters in the  $\beta$ - $T$  plane, causing the observed image of the parameters in the  $\beta$ - $T$  plane to be a blurred version of the true image. If all pixels or sources have the same value of  $\beta$  and  $T$ , then the image of the true values in the  $\beta$ - $T$  plane is that of a ‘pointsource’, and the image of the estimated values is just the banana-shaped ‘PSF’ (i.e., the error distribution). If there is any spread in the  $\beta$  and  $T$  values, then the true image in the  $\beta$ - $T$  plane is that of an ‘extended source’. In order to effectively estimate the image of the true distribution of the parameters in the  $\beta$ - $T$  plane, it is necessary to deconvolve the image of the observed distribution with the error distribution. As we will show in § 2.3, the methods which employ  $\chi^2$ -based estimates implicitly assume that the distribution of the parameters in the  $\beta$ - $T$  plane is uniform over all possible values. Similarly, non-hierarchical Bayesian methods which treat the pixels or sources independently also employ this assumption. Because of the assumption of a uniform distribution, the non-hierarchical methods are not able to deconvolve the image of the estimates in the  $\beta$ - $T$  plane from the error distribution as both the image of the true and estimated distribution are expected to look the same under this assumption. Therefore, both the  $\chi^2$  and non-hierarchical Bayesian methods do not recover the true image of the distribution and are biased. However, the hierarchical modeling framework is able to do the deconvolution because it also employs a model for the ‘source’ image, i.e., the image of the true distribution in the  $\beta$ - $T$  plane. Therefore, the hierarchical model significantly improves on the simpler methods, and provides more accurate estimates of the  $\beta$ - $T$  distribution.

Another advantage of hierarchical modeling is that it is possible to divide the measurement process into multiple levels. This therefore enables us to treat both additive measurement noise and multiplicative calibration errors. Traditional methods usually assume a simple single-level measurement model, and dealing with multiple kinds of measurement error can be difficult for these approaches. However, it is easy to develop a hierarchical model which appropriately treats multiple levels or sources of measurement error.

In this work, we develop a hierarchical model for the analysis of far-IR SEDs of astronomical dust. We perform Bayesian inference on our model, as the uncertainties at all levels of the model are exact and straightforward to interpret under the Bayesian approach. While it is also possible to perform frequentist inference using a hierarchical model, we do not do this as the uncertainties on the estimated quantities are harder to estimate and interpret. Moreover, hierarchical models lend themselves naturally to MCMC algorithms, so Bayesian methods are also computationally straight-forward.

## 2.2. The Measurement Model

We model the dust SED as a modified black body, given by Equation (1). In addition, we multiply Equation (1) by a ‘color-correction’ factor, which corrects the measured flux values for the varying SED across the photometric band, and, if available, is usually given in a tabulated form in the observer’s manual for an instrument. The color-correction factor is given as a function of  $\beta$  and  $T$ .

The SED formulated by Equation (1) is applicable to optically thin dust emission along lines-of-sight with a single temperature. Consequently, sources with a significant amount of high-density material where dust becomes optically thick, and/or with large temperature gradients, will exhibit SEDs which cannot be accurately described by Equation (1). We will modify our technique in future work to implement a more realistic model for the SED in such cases; however, we note that the goal of this paper is to develop a method that minimizes the effects of statistical error on the scientific conclusion, and therefore isolates the systematic errors, allowing for more direct investigations into their effects. We address the issue of systematic errors from inappropriate application of Equation 1 further in Section 5.

For  $j = 1, \dots, m$  observing bands, a map is measured for the source having  $i = 1, \dots, n$  pixels. Denote the frequency of the  $j^{\text{th}}$  band as  $\nu_j$ , and denote the measured flux density for the  $i^{\text{th}}$  pixel observed at  $\nu_j$  as  $\hat{S}_{ij}$ . Assuming Equation (1), the measured flux densities are assumed to be related to the actual values according to the measurement equation

$$\hat{S}_{ij} = \delta_j S_{\nu_j}(N_i, \beta_i, T_i) + \epsilon_{ij}. \quad (2)$$

Here,  $\epsilon_{ij}$  is the random measurement error of the flux density due to noise at frequency  $\nu_j$  for the  $i^{\text{th}}$  pixel, and  $\delta_j$  is the calibration error for the band corresponding to  $\nu_j$ . Note that the calibration error is assumed to be positive and the same for each pixel in the  $j^{\text{th}}$  band.

We assume that the noise is independent between pixels in the same map and over different observing bands, and independent of the calibration uncertainties. In addition, we assume that the calibration errors are independent over the bands. Our assumption that the noise is independent between bands and independent of the calibration error is likely true. However, it is not true that the noise is independent between pixels in the same band. This is because all images are smoothed to the same resolution, therefore correlating the noise in nearby pixels. While this can in theory be accounted for, it is difficult to include in our statistical model and even more difficult to develop an efficient MCMC sampler that accounts for this. Therefore, for simplicity we ignore the correlations in the noise among neighboring pixels. In addition, the calibration errors are often correlated, and therefore our assumption that they are independent may be incorrect. However, for simplicity, and because a quantified summary of the correlations in  $\delta_j$  is typically not available, we assume the calibration uncertainties are independent.

We employ a robust statistical model for the measurement errors and calibration uncertainties. This is to ensure that our conclusions are not severely affected by our assumptions regarding these errors, as robust models allow for outliers and other deviations from the modeling assumptions. We model the distributions of  $\epsilon_{ij}$  and

$\log \delta_j$ , denoted as  $p(\epsilon_{ij})$  and  $p(\log \delta_j)$ , respectively, as having a Student's  $t$ -distribution with degrees of freedom  $d_{\text{meas}}$  and  $d_{\text{cal}}$ , zero mean, and scale parameters  $\sigma_{ij}$  and  $\tau_j$ . The distribution of the measurement noise is then

$$p(\epsilon_{ij}) = \frac{\Gamma((d_{\text{meas}} + 1)/2)}{\Gamma(d_{\text{meas}}/2) \sqrt{d_{\text{meas}} \pi \sigma_{ij}^2}} \left( 1 + \frac{\epsilon_{ij}^2}{\sigma_{ij}^2 d_{\text{meas}}} \right)^{-(d_{\text{meas}}+1)/2} \quad (3)$$

and the distribution of the calibration errors is

$$p(\log \delta_j) = \frac{\Gamma((d_{\text{cal}} + 1)/2)}{\Gamma(d_{\text{cal}}/2) \sqrt{d_{\text{cal}} \pi \tau_j^2}} \left( 1 + \frac{(\log \delta_j)^2}{\tau_j^2 d_{\text{cal}}} \right)^{-(d_{\text{cal}}+1)/2}. \quad (4)$$

Here,  $\Gamma(\cdot)$  is the Gamma Function. In this work we assume  $d_{\text{meas}} = 3$  and  $d_{\text{cal}} = 3$ . The scale parameters,  $\sigma_{ij}$  and  $\tau_j$ , define the amplitude of the noise and calibration error distributions, respectively. In the limit that  $d \rightarrow \infty$ , Equations (3) and (4) converge to a Gaussian distribution with standard deviations  $\sigma_{ij}$  and  $\tau_j$ , respectively. However, unlike the Gaussian distribution, the  $t$ -distribution has more probability in the tails of the distribution, making it robust against outliers; indeed, a  $t$ -distribution is commonly used when one requires a robust statistical model (e.g., Gelman et al. 2004).

The  $t$ -distribution is often appropriate when the measurement errors are assumed to be Gaussian, but their variance is only estimated and therefore unknown. In this case, the  $t$ -distribution also incorporates our uncertainty on the amplitude of the noise and calibration errors. For example, modeling  $\epsilon_{ij}$  as following a Student's  $t$ -distribution corresponds to assuming that the noise is Gaussian with standard deviation  $\tilde{\sigma}_{ij}$ , but we estimate  $\tilde{\sigma}_{ij}$  with  $\sigma_{ij}$ . This is an appropriate model as the values of  $\sigma_{ij}$  are typically estimated from the maps themselves, e.g., by taking the dispersion in the pixel values in a region of the image relatively free of emission. The amplitude of the calibration uncertainties,  $\tau_j$ , are usually available from an observer's manual, but still have some uncertainty associated with them as they are often estimated by comparing a model fit to a calibration source.

When we assume that the unknown  $\tilde{\sigma}_{ij}^2$  follows a Scaled Inverse- $\chi^2$  distribution<sup>4</sup> with  $d_{\text{meas}}$  degrees of freedom and scale parameter  $\sigma_{ij}^2$ , then  $\epsilon_{ij}$  marginally follows a Student's  $t$ -distribution with  $d_{\text{meas}}$  degrees of freedom and scale parameter  $\sigma_{ij}^2$ . In other words, Equation (3) is equivalent to the following:

$$\epsilon_{ij} | \tilde{\sigma}_{ij}^2 \sim N(0, \tilde{\sigma}_{ij}^2) \quad (5)$$

$$\tilde{\sigma}_{ij}^2 \sim \text{Inv-}\chi^2(d_{\text{meas}}, \sigma_{ij}^2). \quad (6)$$

Here, the notation  $x|y \sim p(x|y)$  means that given  $y$ ,  $x$  is drawn from the conditional probability distribution of  $x$  given  $y$ ,  $p(x|y)$ . In addition,  $N(\mu, V)$  is a Gaussian distribution with mean  $\mu$  and variance  $V$ , and  $\text{Inv-}\chi^2(f, s^2)$  is a scaled Inverse- $\chi^2$  distribution with  $f$  degrees of freedom and scale parameter  $s$ .

<sup>4</sup> The Inverse- $\chi^2$  distribution is very similar to a  $\chi^2$  distribution and is commonly used to represent uncertainty in a variance parameter.

In Figure 1 we show the scaled Inverse- $\chi^2$  distribution with 3 degrees of freedom. In addition, we compare the  $t$ -distribution with 3 degrees of freedom to a Gaussian distribution. We chose a value of  $d_{\text{meas}} = d_{\text{cal}} = 3$  for our measurement error model because it is the smallest value for the degrees of freedom that ensures that the Student's  $t$ -distribution has a finite mean and variance. A value of 3 degrees of freedom implicitly assumes that  $\sim 6\%$  of the data will be outliers by more than  $3\sigma$ . Alternatively, a value of 3 degrees of freedom can be interpreted as assuming a factor of  $\sim 2$  uncertainty on the amplitude of the noise. While this may be somewhat excessive, we prefer this conservative approach to make our results robust against inaccuracies in our statistical model, as well as unknown systematic effects. This robustness is illustrated in Figure 1, which shows that outliers are expected in the  $t$  measurement error model as opposed to the Gaussian model, and the outliers are therefore down-weighted to ensure that they do not have an excessive influence on the results. The results are not strongly affected by changes in the degrees of freedom which are less than an order of magnitude, and values of  $d < 10$  are typical for robust models (e.g., Gelman et al. 2004).

### 2.3. The Distribution Model and Posterior Distribution

In this section we derive the probability distribution for the individual values of  $N_i, T_i, \beta_i$ , and the parameters for their joint distribution, given a set of measured dust maps, assuming the measurement model in § 2.2. This is called the ‘posterior distribution’, and is the basis for our Bayesian approach. In order to simultaneously estimate the values of  $N, T$ , and  $\beta$  for each pixel, as well as their joint distribution, we introduce the additional step of assuming a parametric form for the joint distribution for  $N, T$ , and  $\beta$ . Denote the set of parameters<sup>5</sup> for the distribution of  $N, T$ , and  $\beta$  for the source as  $\theta$ , and denote the distribution of these quantities as  $p(N, T, \beta | \theta)$ . Then, the posterior distribution is

$$p(\mathbf{N}, \mathbf{T}, \beta, \theta | \hat{\mathbf{S}}) \propto p(\theta) p(\mathbf{N}, \mathbf{T}, \beta | \theta) p(\hat{\mathbf{S}} | \mathbf{N}, \mathbf{T}, \beta), \quad (7)$$

where  $\mathbf{N}, \mathbf{T}$ , and  $\beta$  are vectors containing the values of column density, temperature, and spectral index for the  $n$  pixels,  $\hat{\mathbf{S}}$  is an  $n \times m$  matrix containing the measured flux densities, and  $p(\theta)$  is the prior distribution on  $\theta$ . The term  $p(\hat{\mathbf{S}} | \mathbf{N}, \mathbf{T}, \beta)$  is the likelihood function of the measured data. The quantity  $p(\mathbf{N}, \mathbf{T}, \beta | \theta)$  defines the distribution of  $N, T$ , and  $\beta$ , while the likelihood function  $p(\hat{\mathbf{S}} | \mathbf{N}, \mathbf{T}, \beta)$  is defined by the measurement model for the maps, i.e., how  $N, T$  and  $\beta$  generate the measured flux densities for each map.

The existence of the calibration uncertainties makes calculation of Equation (7) difficult, as there is no analytical form for the likelihood function of the measured data,  $p(\hat{\mathbf{S}} | \mathbf{N}, \mathbf{T}, \beta)$ . However, it is straightforward to calculate the likelihood function for the case of fixed cali-

<sup>5</sup> The notation  $\theta$  is used as a short-hand way of denoting the set of parameters for the distribution of  $N, T$ , and  $\beta$ . Once we choose a particular distribution, then  $\theta$  contains the parameters for this distribution. At this point the derivation is still general so  $\theta$  is left unspecified. Later we will model the distribution of  $\log N, \log T$ , and  $\beta$  as a Student's  $t$ -distribution, so  $\theta = (\mu, \Sigma)$ , where  $\mu$  is the mean vector and  $\Sigma$  is proportional to the covariance matrix.

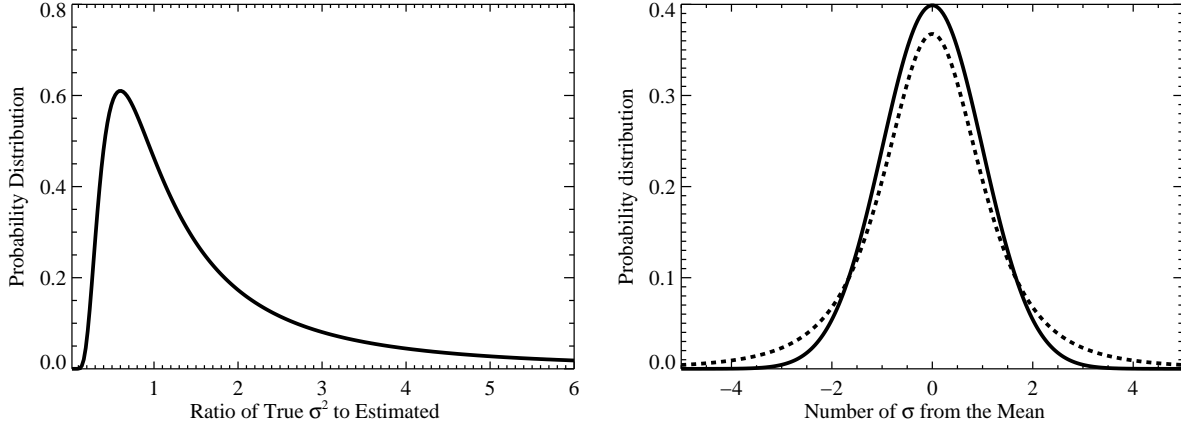


FIG. 1.— The scaled Inverse- $\chi^2$  distribution with  $d = 3$  degrees of freedom (left), and the Student's  $t$ -distribution with  $d = 3$  degrees of freedom (right, dashed line) compared with a Gaussian distribution (solid line). The Student's  $t$ -distribution is appropriate when the errors are assumed to be Gaussian, but the uncertainty on the variances of the errors can be modeled as a scaled Inverse- $\chi^2$  distribution. The additional uncertainty on the amplitude of the errors is reflected in the thicker tails of the  $t$ -distribution, making the  $t$ -model more robust against outliers. In this work we model both the measurement noise and calibration uncertainties as following a Student's  $t$ -distribution with  $d_{\text{meas}} = 3$  and  $d_{\text{cal}} = 3$  degrees of freedom for the measurement noise and calibration uncertainties, respectively, as the amplitudes of both the noise and calibration errors are only estimated; the  $t$ -model therefore makes our method robust against outliers.

bration uncertainty,  $p(\hat{\mathbf{S}}|\mathbf{N}, \mathbf{T}, \beta, \delta)$ . For our  $t$  model for the measurement noise, the likelihood function at fixed  $\delta$  is

$$p(\hat{S}_{ij}|N_i, T_i, \beta_i, \delta_j) \propto \frac{1}{\sigma_{ij}} \left[ 1 + \frac{(\hat{S}_{ij} - \delta_j S_{\nu_j}(N_i, \beta_i, T_i))^2}{\sigma_{ij}^2 d_{\text{meas}}} \right]^{-(d_{\text{meas}}+1)/2}. \quad (8)$$

The actual measured data likelihood function,  $p(\hat{\mathbf{S}}|\mathbf{N}, \mathbf{T}, \beta)$ , is then obtained by averaging  $p(\hat{\mathbf{S}}|\mathbf{N}, \mathbf{T}, \beta, \delta)$  over the distribution of  $\delta$ . Therefore, in order to derive Equation (7), we first start with the posterior distribution that we would have obtained if we treated the calibration uncertainties as additional parameters:

$$p(\mathbf{N}, \mathbf{T}, \beta, \theta, \log \delta | \hat{\mathbf{S}}) \propto p(\theta) \left[ \prod_{i=1}^n p(N_i, T_i, \beta_i | \theta) \right] \prod_{j=1}^m \left[ p(\log \delta_j) \prod_{i=1}^n p(\hat{S}_{ij} | N_i, T_i, \beta_i, \delta_j) \right]$$

Then, Equation (7) is obtained by integrating Equation (9) over  $\log \delta_j$  for  $j = 1, \dots, m$ .

In this work we model the distribution of  $\log N$ ,  $\log T$ , and  $\beta$  as a multivariate Student's  $t$ -distribution with  $d = 8$  degrees of freedom:

$$p(\log N_i, \log T_i, \beta_i | \mu, \Sigma) \propto \frac{1}{|\Sigma|^{1/2}} \left[ 1 + \frac{1}{d} (\mathbf{x}_i - \mu)^T \Sigma^{-1} (\mathbf{x}_i - \mu) \right]^{-(d+3)/2} \quad (10)$$

$$\mathbf{x}_i = (\log N_i, \log T_i, \beta_i). \quad (11)$$

Here,  $\mathbf{x}^T$  denotes the transpose of  $\mathbf{x}$ ,  $\theta = (\mu, \Sigma)$ ,  $\mu$  is the model mean value of  $(\log N, \log T, \beta)$ , and  $\Sigma$  is proportional to the model covariance matrix of  $(\log N, \log T, \beta)$ . Our reasons for using  $d = 8$  are similar to the case of modeling the measurement errors; we want to use a distribution that is robust against outlying values of  $N, T$ , or  $\beta$ . A value of  $d = 8$  implies that we expect about  $\sim 1.6\%$  of the data to be outliers by more than  $3\sigma$ . We

consider this to be a reasonable choice, but as with the measurement model, our results are not strongly affected by the choice of  $d$ . Under the  $t$ -model, one can now use Equations (8)–(11) in combination with Equation (4) and a prior distribution  $p(\theta)$  to calculate the posterior distribution.

In this work we assume a uniform prior on  $\mu$ . For the prior on  $\Sigma$ , we use the so-called ‘separation strategy’ prior developed by Barnard et al. (2000). This prior is based on the decomposition

$$\Sigma = SRS, \quad (12)$$

where  $S$  is the diagonal matrix of standard deviations and  $R$  is the correlation matrix. The separation strategy works by placing independent priors on the standard deviations and correlations. In this work we place a normal prior on the elements of  $\log S$  centered at the values inferred from the  $\chi^2$  estimates with variance equal to 100; this is an extremely broad prior giving nearly equal weight to most reasonable values of the dispersion in  $\log N, \beta$ , and  $\log T$ . Following Barnard et al. (2000), we place an inverse-Wishart prior on  $R$  with four degrees of freedom. Under this choice of prior, the marginal prior distributions for the correlations between  $\log N, \beta$ , and  $\log T$  are uniform over  $[-1, 1]$ , reflecting our prior assumption that all values of the correlations are equally likely.

The traditional non-hierarchical methods can be derived as a special case under our hierarchical Bayesian model. When the errors are assumed to be Gaussian ( $d \rightarrow \infty$ ), one ignores calibration uncertainties ( $\delta_j = 1$ ), and when one assumes that  $\log N, \log T$ , and  $\beta$  are independently and uniformly distributed over all possible values ( $\Sigma \rightarrow \infty$ ), the posterior distribution becomes

$$p(\mathbf{N}, \mathbf{T}, \beta | \hat{\mathbf{S}}) \propto \prod_{i=1}^n \exp(-\chi_i^2/2), \quad (13)$$

where

$$\chi_i^2 = \sum_{j=1}^m \left[ \frac{\hat{S}_{ij} - S_{\nu_j}(N_i, \beta_i, T_i)}{\sigma_{ij}} \right]^2. \quad (14)$$

If the estimated values of  $N$ ,  $T$ , and  $\beta$  are constrained to fall within some range, say  $0 < \beta < 5$ , then Equation (13) is derived from the assumption of a uniform distribution over this range. Under Equation (13) the values of  $N_i$ ,  $T_i$ , and  $\beta_i$  are independent in their posterior probability distribution, and thus their best-fit values can be obtained independently for each pixel. The  $\chi^2$ -based estimators are those that maximize the posterior distribution under the simplifying assumptions that the errors are Gaussian, that there are no calibration uncertainties, and that  $\log N$ ,  $\log T$ , and  $\beta$  are independently and uniformly distributed over all possible values. Similarly, non-hierarchical Bayesian methods based on Equation (13) also make these same assumptions (Paradis et al. 2010). However, it is not true that all three of these assumptions hold. In particular, the assumption that  $\log N$ ,  $\log T$ , and  $\beta$  are independently and uniformly distributed over some range of values is a very strong assumption and leads to estimates of these quantities that are independent for each pixel, and thus the estimated quantities are overdispersed compared to their true values. This overdispersion biases the inferred correlation between  $\beta$  and  $T$  toward an anti-correlation, such as that described by Shetty et al. (2009a). Indeed, the very fact that an anti-correlation between  $\beta$  and  $T$  is inferred from such methods shows that their assumption of statistical independence is violated, as statistically independent quantities must be uncorrelated. Therefore, such methods are not self-consistent. Our hierarchical Bayesian approach significantly ameliorates these problems by using a more realistic model for the distribution of  $\log N$ ,  $\log T$ , and  $\beta$ , for the measurement errors, and by including the calibration uncertainties.

The posterior distribution, given by Equation (7), completely summarizes our information on  $\mathbf{N}$ ,  $\mathbf{T}$ ,  $\beta$ ,  $\mu$ , and  $\Sigma$ . We can then use Equation (7) to compute estimates of these parameters, and summarize our uncertainty on  $\mu$  and  $\Sigma$ . However, there are a large number of parameters involved in Equation (7), as each source is assumed to have its own value of  $N$ ,  $T$ , and  $\beta$ . Therefore, we will not be able to compute Equation (7) on a grid, as there are  $3n+9$  free parameters. Because of this, we employ MCMC methods to obtain a set of random draws of  $\mathbf{N}$ ,  $\mathbf{T}$ ,  $\beta$ ,  $\mu$ , and  $\Sigma$  from the posterior distribution. In addition, it is difficult, if not impossible, to analytically integrate Equation (9) over each  $\delta_j$ , which is necessary in order to compute Equation (7). For large values of  $n$ , it is computationally intensive to do the integration over  $\log \delta_j$  numerically because of the product over the  $n$  data points. In order to make the computation of the posterior distribution tractable, we instead consider the unknown values of the calibration errors,  $\delta_j$ , to be additional parameters and work directly with Equation (9) instead of Equation (7). Under this strategy, the values of  $\log \delta_j$  are additional parameters that are also estimated at each stage of our MCMC sampler. However, because the values of the calibration errors are of no scientific interest (i.e.,  $\delta_j$  is a ‘nuisance’ parameter), we simply discard the values of  $\log \delta_j$  returned by our MCMC sampler, thus marginalizing over them. The result is a set of random draws of  $\mathbf{N}$ ,  $\mathbf{T}$ ,  $\beta$ , and  $\theta$  from Equation (7).

We construct our MCMC sampler using a combination of Metropolis-Hastings updates and Gibbs sampling, where the Gibbs updates are used whenever possible. In

addition, to remove degeneracies in some of the parameters, and thus to increase the efficiency of our MCMC sampler, we employ an Ancillarity-Sufficiency Interweaving Strategy (Yu & Meng 2011) with respect to the calibration uncertainties. Implementing the interweaving strategy is necessary as we could not get our MCMC sampler to converge without implementing it. Further technical details of our MCMC sampler are given in Kelly (2011). All statistical inference is then done using the random samples of  $\mathbf{N}$ ,  $\mathbf{T}$ ,  $\beta$ ,  $\mu$ , and  $\Sigma$  generated from our MCMC algorithm.

Before concluding this section, we wish to make a comment on the sensitivity of the Bayesian fits to the assumed population model. The true distribution for  $\log N$ ,  $\log T$ , and  $\beta$  is unlikely to follow a  $t$ -distribution (or Gaussian, for that matter), but it is unlikely that errors due to this mismatch will have a significant effect on our results. This is because we are primarily interested in the moments of the data (e.g., the correlation between  $T$  and  $\beta$ ), and simple models such as the  $t$ -distribution often enable us to adequately recover them. Moreover, most of our analysis relies on analyzing the values of  $N_i$ ,  $T_i$ , and  $\beta_i$  returned by our MCMC sampler, which have their values ‘corrected’ relative to the  $\chi^2$ -based estimates under the assumption that they come from a common distribution, which we assume can be approximated as a  $t$ -distribution. The degree to which the values of  $N$ ,  $T$ , and  $\beta$  are corrected for any given pixel depends on the  $S/N$  of that pixel. When the  $S/N$  is high, the correction is small as the information on the values of  $N_i$ ,  $T_i$ , and  $\beta_i$  is dominated by the information from the data. In this case, the estimated values of  $N_i$ ,  $T_i$ , and  $\beta_i$  for that pixel are insensitive to the choice of model for the joint distribution and will be similar to those obtained by minimizing  $\chi^2$ . By focusing our analysis on the values of  $\mathbf{N}$ ,  $\mathbf{T}$ , and  $\beta$  that are returned by our Bayesian approach, instead of the values of  $\mu$  and  $\Sigma$ , we are less sensitive to differences between our model and the true distribution. In general, so long as the distribution of  $N$ ,  $T$ , and  $\beta$  does not exhibit multiple modes separated by large distances, the scientific conclusions should not be very sensitive to error due to misspecifying the statistical model. We further explore this issue in the following section.

### 3. TESTS OF HIERARCHICAL BAYESIAN METHOD ON SIMULATED DATA

In order to illustrate the effectiveness of our Bayesian approach, and its improvement over traditional  $\chi^2$ -based techniques, we apply our method to two simulated data sets. The first simulated data set is a source with mean  $T \sim 20$  K, and the second is a source with mean  $T \sim 80$  K. We simulate values of the quantity  $C = N\Omega\kappa_0$  from a mixture of two log-normal distributions:

$$p(\log C) = \pi\phi(\log C|\bar{C}_1, v_1^2) + (1 - \pi)\phi(\log C|\bar{C}_2, v_2^2). \quad (15)$$

Here,  $\phi(\log C|\bar{C}, v^2)$  denotes a Gaussian distribution with mean  $\bar{C}$  and variance  $v^2$  as a function of  $\log C$ . For both the cooler and warmer source we set  $\pi = 0.4$ ,  $\bar{C}_1 = 7.6$ ,  $\bar{C}_2 = 8.6$ ,  $v_1 = 0.4$ , and  $v_2 = 0.15$ . These values were chosen to give column densities similar to that observed for CB 244 as observed by *Herschel*, which we analyze in § 4. We simulate values of temperature from a mixture

of two Gamma distributions:

$$p(T) = \pi\Gamma(T|k_1, T_1^*) + (1 - \pi)\Gamma(T|k_2, T_2^*). \quad (16)$$

Here,  $\Gamma(T|k, T^*)$  is a Gamma distribution with shape parameter  $k$  and scale parameter  $T^*$  as a function of  $T$ ; note that the mean and standard deviation of the Gamma distribution is  $T^*k$  and  $T^*\sqrt{k}$ , respectively. For the cooler simulated source we set  $k_1 = 500, T_1^* = 0.03, k_2 = 100$ , and  $T_2^* = 0.2$ . For the hotter simulated source we set  $k_1 = 500, T_1^* = 0.15, k_2 = 1000$ , and  $T_2^* = 0.08$ . Finally, for both sources we simulated values of  $\beta$  at fixed temperature from a Gaussian distribution with mean  $A+B\log T$  and standard deviation 0.1. We set  $B = 0.5$ , and  $A$  is chosen to give a mean value of  $\langle\beta\rangle = 2$ . In our simulations  $\beta$  and  $T$  are weakly and positively correlated by construction.

We note that our model of a Student's  $t$ -distribution for the joint distribution of  $\log N, \log T$ , and  $\beta$  is violated in these simulations. In fact, the distribution of  $\log N$  is bimodal, as is the distribution of  $\log T$  for the cooler simulated source. These simulations will provide a good test of the sensitivity of our results to our assumption of a Student's  $t$ -distribution for  $(\log N, \log T, \beta)$ .

We simulated flux values for  $n = 1000$  data points at observational wavelengths  $\lambda = 100, 160, 250, 350$ , and  $500 \mu\text{m}$ , corresponding to those employed by the *PACS* and *SPIRE* instruments onboard *Herschel*. We multiplied the flux points in each band by a constant calibration error; the calibration errors were the same for every pixel in a given band, but differed over the five bands. The calibration errors were drawn from a log-normal distribution with standard deviations of 2.75%, 4.15%, 7%, 7%, and 7% for each band, respectively. These values were chosen to be equal to the official calibration uncertainties for *PACS* and *SPIRE* for a point source. To all fluxes, we also added noise drawn from Gaussian distributions with standard deviations  $\sigma_j = [2.2, 3.3, 5.2, 3.7, 2.2] \times 10^{-5} \text{ Jy arcsec}^{-2}$  for each of the five bands, respectively. These values were chosen to be similar to those observed in the *Herschel* observation of CB244 (Stutz et al. 2010), which we apply our method to in § 4.2; see § 4.1 for further details. The signal-to-noise distribution for the source with mean  $T \sim 20 \text{ K}$  is similar to that of the *Herschel* observations of CB244. For this source, most of the pixels have uncertainties dominated by the measurement noise, while the high  $S/N$  have uncertainties dominated by the calibration errors. However, most pixels for the source with mean  $T \sim 80 \text{ K}$  have uncertainties dominated by the calibration errors. Therefore, the warmer source also provides an interesting test regarding the importance of accounting for the calibration uncertainties.

We applied both our Bayesian method and a  $\chi^2$ -based method to the two simulated data sets. For the  $\chi^2$  fits, we constrained the best-fit temperature values to be between  $1 < T < 100$  for the cooler source and  $1 < T < 300$  for the warmer source. We constrained the column density to be positive and  $\beta$  to lie within  $-10 < \beta < 10$  for both sources. For each data point, we chose five random independent initial guesses for  $N, T$ , and  $\beta$ , and ran our  $\chi^2$  minimizer on each, keeping the value that minimized  $\chi^2$  over the initial guesses. It is necessary to randomly initialize the  $\chi^2$  minimizing algorithm at multiple starting locations because the algorithm did not always converge,

or there may have been local minima; this is mostly a problem for the low  $S/N$  data points. For the cooler source, we remove 104 data points for which the  $\chi^2$  fits converged to a value on the boundary. For the warmer source, we only exclude 2 data points which converged to the boundary.

In Figures 2 and 3 we show a random draw of the values of  $\beta$  and temperature for each pixel from their posterior probability distribution for the source with mean  $T \sim 20 \text{ K}$  and  $T \sim 80 \text{ K}$ , respectively. We plot a random draw of  $\beta$  and  $T$  instead of the posterior median or mean because the random draw of  $\beta$  and  $T$  more accurately reflects the spread of the data in the  $\beta$ - $T$  plane. While the posterior median or mean values provide better estimates of  $\beta$  and  $T$  for any individual pixel, the distribution of their values does not reflect as good of an estimate of the distribution of  $\beta$  and  $T$ , as they average over the intrinsic variability in these quantities that is present in every draw from the posterior distribution. In both Figures we also show the distribution of the best-fit values obtained from minimizing  $\chi^2$ . In agreement with Shetty et al. (2009a), we find that the distributions for both  $\beta$  and  $T$  of the  $\chi^2$ -based estimates are wider than the true distributions. Furthermore, *the distribution of the  $\chi^2$ -based estimates for  $\beta$  and  $T$  portrays an anti-correlation between these two quantities, despite the fact that these two quantities are constructed to be positively correlated in our simulations.* This occurs because the  $\chi^2$ -based estimate of the  $\beta$ - $T$  relationship is always biased toward an anti-correlation, as the errors in  $\beta$  and  $T$  estimated by minimizing  $\chi^2$  are anti-correlated. For this simulation the errors on the  $\chi^2$ -based estimates are large, and the magnitude of this bias is large enough to reverse the sign of the correlation.

In Table 1 we compare the true values of the Spearman's rank correlation between  $\beta$  and  $T$  for both simulations, denoted as  $\rho$ , with those obtained from the  $\chi^2$ -based estimators and that obtained from our hierarchical Bayesian method. In addition, in Table 1 we compare the average values for  $T$  and  $\beta$ , and compare the values of the correlations and standard deviations of the best-fit parameters; for the Bayesian estimates we use the values of the correlations and standard deviations derived from the model covariance matrix to investigate how well the model covariance matrix recovers the true values. Unlike the  $\chi^2$ -based estimators, the best-fit estimates derived using our hierarchical Bayesian method provide a more faithful reconstruction of the intrinsic distribution of  $\beta$  and  $T$ . In particular, the Bayesian estimates recover the true positive correlation between  $\beta$  and  $T$ .

Our Bayesian method correctly recovers the true values of the means and correlation coefficients within the uncertainties. The only exception to this is the mean temperature for the warmer source, for which our Bayesian method overestimates the true value by  $\approx 4 \text{ K}$ , a difference of about 5%. This bias is most likely caused by our incorrect assumption of a Student's  $t$ -distribution for the intrinsic distribution of  $(\log N, \log T, \beta)$ . However, this bias is very small, and in general our Bayesian approach recovers the correct values, illustrating the robustness of our method to inaccuracies in the assumed distribution. In contrast, the distribution derived from the  $\chi^2$ -based estimates is biased and leads to incorrect conclusions. In addition to a spurious anti-correlation



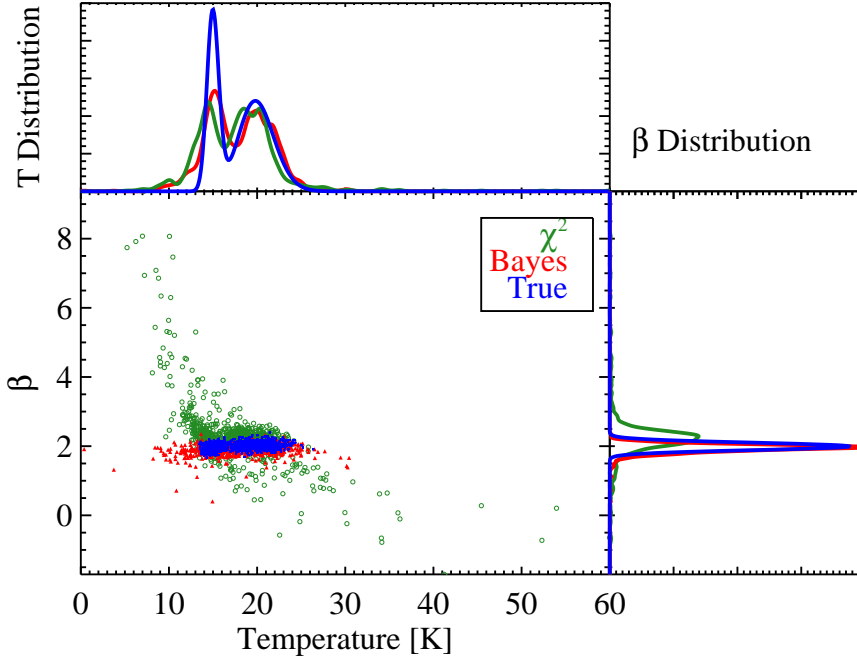


FIG. 2.— Distribution of the true values for  $\beta$  and  $T$  (blue squares) for a simulated source with mean  $T \sim 20$  K, compared with a random draw from the posterior distribution using our Bayesian hierarchical model (red triangles) and  $\chi^2$ -based (green open circles) estimates. Also shown are the marginal distributions for temperature (top) and  $\beta$  (right) for the true values (blue), Bayesian estimates (red), and  $\chi^2$  estimates (green). For clarity one data point with a  $\chi^2$ -based estimate of  $T > 60$  K is excluded. The Bayesian estimates more accurately recover the true distribution of  $\beta$  and  $T$  and their correlation, while the  $\chi^2$ -based estimates incorrectly show an anti-correlation and exhibit some bias in estimating the average  $\beta$ .

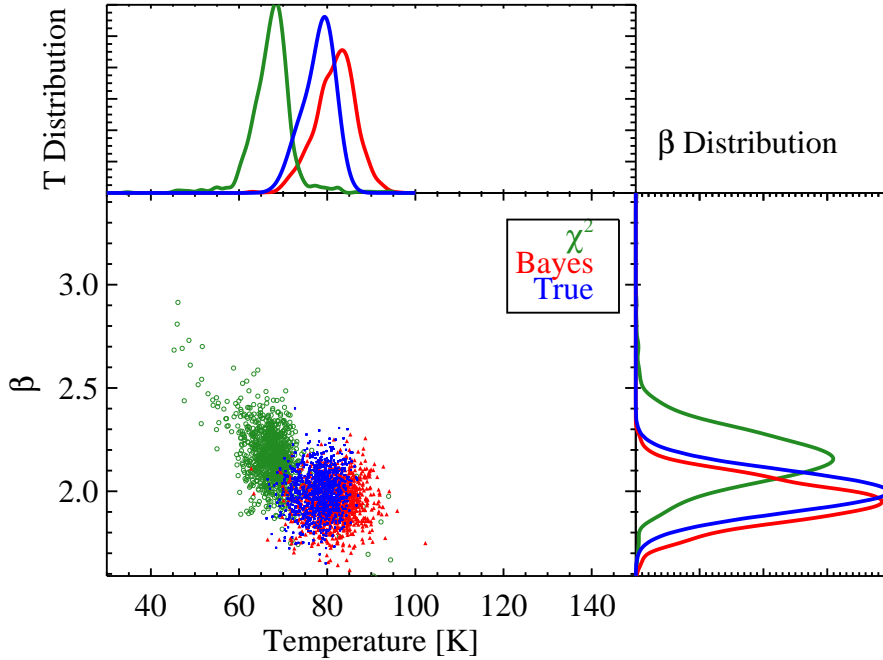


FIG. 3.— Same as Figure 2, but for a simulated source with mean  $T \sim 80$  K. For clarity, two sources with  $\chi^2$ -based estimates of  $T > 150$  K are excluded. As with the cooler source, our hierarchical Bayesian estimates provide a better reconstruction of the true distribution, although they exhibit a small bias in the estimated average temperature. In contrast, the  $\chi^2$  estimates incorrectly imply a weak anti-correlation between  $\beta$  and  $T$ , and exhibit some bias in the average values of  $\beta$  and  $T$ .

TABLE 1  
COMPARISON OF PERFORMANCE OF  $\chi^2$ -BASED ESTIMATORS WITH HIERARCHICAL BAYESIAN ESTIMATES ON  
SIMULATED DATA WITH  $T \sim 20$  K AND  $T \sim 80$  K

	Cooler Source			Warmer Source		
	True	$\chi^2$	Bayes	True	$\chi^2$	Bayes
$\rho^a$	0.33	$-0.45 \pm 0.03$	$0.23 \pm 0.08$	0.10	$-0.34 \pm 0.03$	$0.07 \pm 0.02$
$\bar{\beta}^b$	2.0	$2.26 \pm 0.03$	$1.90 \pm 0.07$	2.0	$2.16 \pm 0.01$	$1.96 \pm 0.04$
$\bar{T}^c$	18.0	$17.8 \pm 0.17$	$18.3 \pm 0.3$	78.0	$67.8 \pm 0.25$	$81.9 \pm 0.18$
$\text{Corr}(\log N, \beta)^d$	-0.02	$-0.61 \pm 0.02$	$0.00 \pm 0.06$	-0.01	$-0.07 \pm 0.03$	$0.01 \pm 0.04$
$\text{Corr}(\log T, \beta)^e$	0.32	$-0.69 \pm 0.02$	$0.38 \pm 0.03$	0.09	$-0.62 \pm 0.02$	$0.08 \pm 0.03$
$\text{Corr}(\log N, \log T)^f$	-0.04	$0.21 \pm 0.03$	$-0.06 \pm 0.03$	-0.01	$0.00 \pm 0.03$	$-0.01 \pm 0.04$
$\sigma(\log N)^g$	0.55	$0.59 \pm 0.01$	$0.58 \pm 0.02$	0.56	$0.58 \pm 0.01$	$0.60 \pm 0.01$
$\sigma(\beta)^h$	0.10	$0.90 \pm 0.02$	$0.111 \pm 0.001$	0.10	$0.15 \pm 0.01$	$0.11 \pm 0.01$
$\sigma(\log T)^i$	0.07	$0.109 \pm 0.002$	$0.083 \pm 0.001$	0.02	$0.04 \pm 0.001$	$0.03 \pm 0.001$

<sup>a</sup> The value of Spearman's rank correlation coefficient between  $\beta$  and  $T$  for the simulated sources.

<sup>b</sup> The average value of  $\beta$  for the simulated sources.

<sup>c</sup> The average value of temperature for the simulated sources.

<sup>d</sup> The model value for the correlation between  $\log N$  and  $\beta$

<sup>e</sup> The model value for the correlation between  $\log T$  and  $\beta$

<sup>f</sup> The model value for the correlation between  $\log N$  and  $\log T$

<sup>g</sup> The model value for the standard deviation in  $\log N$ .

<sup>h</sup> The model value for the standard deviation in  $\beta$ .

<sup>i</sup> The model value for the standard deviation in  $\log T$ .

between  $\beta$  and  $T$ , the  $\chi^2$ -based estimates also exhibit biases in the estimated mean values of  $\beta$  and  $T$ . The  $\chi^2$ -based method correctly recovers the mean temperature for the cooler source, but overestimates the mean value of  $\beta$  by  $\approx 13\%$ . The bias in the mean values is more noticeable for the warmer source, where the fluxes only sample the Rayleigh-Jeans regime. Here, the mean  $\beta$  is overestimated by  $\approx 8\%$  while the mean temperature is underestimated by  $\approx 15\%$ . The most likely source of this bias is the calibration errors, which the  $\chi^2$  method does not account for. In contrast, our Bayesian approach corrects for the calibration errors, and incorporates their contribution to the uncertainty in the parameters estimates.

Our hierarchical Bayesian method also does a better job of recovering the true values of  $N$ ,  $\beta$ , and  $T$  for individual pixels. For the cooler source the median absolute values of the error in the Bayesian estimates for  $\log N$ ,  $\beta$ , and  $T$  are 0.05, 0.11, and 0.59, respectively. For the  $\chi^2$  estimates, these values are 0.08, 0.25, and 1.08 for  $\log N$ ,  $\beta$ , and  $T$ . The Bayesian posterior median estimates do a factor of  $\approx 2$  better than the  $\chi^2$  estimates for the source with mean  $T \sim 20$  K. For the source with mean  $T \sim 80$  the Bayesian fits for individual pixels also did better, but this time the error in the  $\chi^2$  estimates are dominated by the bias caused by the unaccounted-for calibration errors.

As a sanity check, we also show that our hierarchical Bayesian method recovers an anti-correlation when one exists. We simulate values of  $\beta$ ,  $T$ , and  $N$  in exactly the same manner as for the source with mean  $T \sim 20$  above, but this time enforce an anti-correlation by using a value of  $B = -0.5$ . We then apply our hierarchical Bayesian method to the simulated data, and obtain estimates via  $\chi^2$ -minimization. Figure 4 compares the results. For this simulation, the true value of the Spearman's rank correlation coefficient between  $\beta$  and  $T$  is  $\rho = -0.28$ . The value inferred from our Hierarchical Bayesian estimate is  $\rho = -0.27 \pm 0.02$ , while the value inferred from the  $\chi^2$ -based estimates is  $\rho = -0.38 \pm 0.03$ . Both the Bayesian and  $\chi^2$  method recover the anti-correlation. However, as expected the  $\chi^2$  estimates produces an artificially stronger and more extended  $T$ - $\beta$  anti-correlation (see Section 2.1).

As a final test of our method we generate fluxes from an idealized simple model of a starless core. We construct a projected core similar to Model 1 from Shetty et al. (2009b), based on work by Evans et al. (2001). In this model,  $N$  increases linearly toward the central regions, ranging from  $2 \times 10^{21}$  to  $1.25 \times 10^{22} \text{ cm}^{-3}$ . Correspondingly,  $T$  decreases linearly, from 12 to 8 K. Lastly,  $\beta$  decreases from 2.6 to 1.8. Our choice of the quantitative values for  $T$ ,  $N$ , and  $\beta$  are motivated by the results we obtain from CB244 (see § 4.2), and are generally consistent with the trends discussed by (Evans et al. 2001). This model provides a test of how our method performs in the limiting scenario where the values of  $N$ ,  $T$ , and  $\beta$  all lie on simple deterministic curves which do not have any intrinsic dispersion. We do not consider this model to be realistic, as a real cloud is unlikely to be spherically symmetric with the line-of-sight averaged values of  $N$ ,  $T$ , and  $\beta$  lying along deterministic curves. However, it does provide a useful test of our method as this model may violate the assumption that the covariance matrix

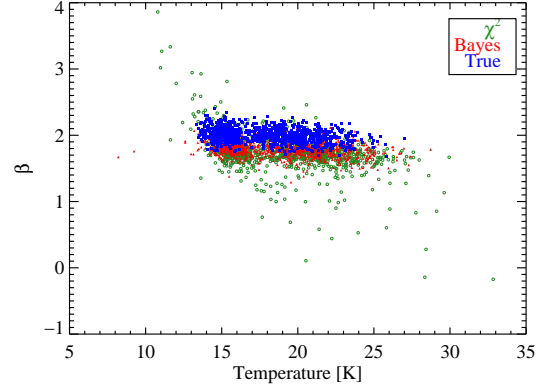


FIG. 4.— Distribution of true values of  $\beta$  and  $T$  (blue square points) for a simulated data set with an intrinsic anti-correlation enforced, compared with the distribution of the  $\chi^2$ -based estimates (green open circles) and a random draw from the posterior distribution under our hierarchical Bayesian model (red triangles). Both methods are able to recover the anti-correlation, but the  $\chi^2$ -based estimates produce a stronger and more extended  $T$ - $\beta$  anti-correlation compared to the true distribution.

of  $(\log N, \log T, \beta)$  is positive definite.

For this model we simulate flux values as before, and execute both our hierarchical Bayesian method and the  $\chi^2$  fit. The true correlation coefficients are  $\text{Corr}(\log N, \beta) = -0.98$ ,  $\text{Corr}(\log N, \log T) = -0.97$ , and  $\text{Corr}(\log T, \beta) = 0.99$ . Our hierarchical Bayesian method returns values of  $\text{Corr}(\log N, \beta) = -0.95 \pm 0.03$ ,  $\text{Corr}(\log N, \log T) = -0.98 \pm 0.001$ , and  $\text{Corr}(\log T, \beta) = 0.88 \pm 0.04$ , while the  $\chi^2$ -based estimates infer  $\text{Corr}(\log N, \beta) = -0.41$ ,  $\text{Corr}(\log N, \log T) = -0.31$ , and  $\text{Corr}(\log T, \beta) = -0.71$ . Our hierarchical Bayesian method again outperforms the  $\chi^2$  approach for this test, although it does not perform as well as in previous tests. In addition, as with the other tests the  $\chi^2$  method incorrectly produces an anti-correlation between  $\beta$  and  $T$ .

For this test, convergence of our MCMC sampler proves to be extremely slow due to the strong dependencies among the values of  $N$ ,  $\beta$ , and  $T$  and  $\Sigma$ . Because the correlations for this test are  $|r| \approx 1$ ,  $N$ ,  $\beta$ , and  $T$  for each pixel are very precisely determined from  $\mu$  and  $\Sigma$ . However, given  $N$ ,  $\beta$ , and  $T$  for each pixel,  $\mu$  and  $\Sigma$  are very precisely determined. This dependency results in very slow convergence of our MCMC sampler, and the decreased performance is likely due to this lack of convergence. While this does not affect the qualitative results, convergence should be carefully monitored when there is evidence that the correlations from  $\Sigma$  converge to 1 or -1. Future additions to our MCMC sampler will improve convergence for cases where the correlations among  $N$ ,  $\beta$ , and  $T$  are extremely tight.

#### 4. APPLICATION: DUST IN STAR FORMING BOK GLOBULE CB244

In this section we discuss the application of our Hierarchical Bayesian method to the Bok globule CB244. The purpose of this application is to illustrate how our method performs on real data, to compare the results from our method with those obtained from  $\chi^2$  minimization, and to illustrate what type of conclusions might be derived from our method as compared to traditional non-hierarchical methods. The application of our method to

CB244 is valuable as an illustration because real data is often subject to further complications beyond the simple idealized simulations that we have performed, and can include a number of systematics that are not captured in our statistical model. A full treatment of all data systematics is beyond the scope of this methodology-focused article, but will be addressed in future work when we apply our method to similar astronomical sources.

#### 4.1. Observations

CB244 is an isolated, low-mass, star-forming molecular cloud located at a distance of  $\sim 200$  pc. It contains two *Herschel* emission peaks, one associated with a Class 0 protostar and one associated with a starless core (Stutz et al. 2010). Because of the relative simple geometry of such sources, Bok globules are excellent targets to study the processes taking place in the dense ISM, free from complications arising in more clustered environments. The *Herschel* CB244 data were acquired as part of the Guaranteed Time Key Programme “Earliest Phases of Star-formation” (EPoS; P.I. O. Krause, e.g.; Beuther et al. 2010; Henning et al. 2010; Linz et al. 2010; Stutz et al. 2010) as part of the Science Demonstration Program. The sources in this program were selected to be in relatively isolated regions in order to minimize the effects from uncertain background subtraction. These data were first presented in (Stutz et al. 2010). The submm SCUBA 870  $\mu\text{m}$  and the IRAM 1.3 mm ground-based data were presented in Launhardt et al. (2010). For our purposes of temperature mapping, the data reduction has been updated; here we present a brief outline of the *Herschel* processing. See Launhardt et al., (2012, in prep) for further details.

The *Herschel* (Pilbratt et al. 2010) data for CB244 were observed with the Photodetector Array Camera and Spectrometer (PACS; Poglitsch et al. 2010) and Spectral and Photometric Imaging Receiver (SPIRE; Griffin et al. 2010). The PACS 100  $\mu\text{m}$  and 160  $\mu\text{m}$  observations were carried out on December 30, 2009. Two orthogonal scan maps were acquired using a scan speed of  $20''/\text{s}$  with scan leg lengths of  $9'$ . The AOR ID's for these observations are 134218869(4,5). The two wavelengths were processed in an identical fashion. The level 1 data were processed using HIPE v. 6.0.1196. Final level 2 maps were produced using Scanamorphos (Roussel et al., 2011, in prep.), using the “galactic” option. These data were processed including the non-zero-acceleration telescope turn-around data. The SPIRE 250, 350, and 500  $\mu\text{m}$  observations were obtained on October 20, 2009. Two  $9'$  scan legs were obtained at the nominal scan speed of  $30''/\text{s}$ . The AOR ID for these data is 1342199366. These data were processed up to level 1 with HIPE 5.0.1892. The level 2 maps were processed using Scanamorphos v.9 (Roussel et al., 2011, in prep.).

The calibrated dust emission maps were then processed in an identical fashion to the data presented in Launhardt et al., (2012, in prep). We briefly summarize the steps used here. First, the data are re-zeroed using a method similar to that applied to *Spitzer MIPS* images in Stutz et al. (2009). In order to calculate the DC-level offset from the data we identified a  $4' \times 4'$  emission-free region that appears ‘dark’ in the *Herschel* maps. In addition, we require that this region is in or near a region which is relatively free from  $^{12}\text{CO}(2-1)$  emission (Laun-

hardt et al. 2012, in prep). The same spatial region was used for all five *Herschel* maps. For each band, we then calculate the representative flux level in the region by implementing an iterative Gaussian function fitting and sigma-clipping scheme to the pixel value distribution at each wavelength. The mean value of the best-fit Gaussian function is subtracted from each image, while the standard deviation is used to estimate the noise levels. If the noise in the image is Gaussian, then the distribution of measured flux values for pixels with true flux near the DC level will also be Gaussian. In this case, the mean of the best-fit Gaussian function provides an estimate of the DC level, while the standard deviation of the best-fit Gaussian function provides an estimate of the noise amplitude. The estimated DC levels and noise levels for each *Herschel* map are reported in Table 2.

A pointing correction is also applied to the PACS images relative to the MIPS 24  $\mu\text{m}$  data of the same field; in the case of CB244 this correction is small (of order  $1''$ ) compared to the SPIRE 500  $\mu\text{m}$  beam. We apply the recent *Herschel* calibration correction factors to the data. The 100 to 500  $\mu\text{m}$  data are then converted to common units of  $\text{Jy}/''^2$ . The data (including the sub-mm ground-based observations) are then convolved to the limiting beam, in this case the SPIRE 500  $\mu\text{m}$  beam. We use the Aniano et al. (2011) circularized convolution kernels for the 100 to 350  $\mu\text{m}$  data, and a Gaussian beam approximation for the ground-based sub-mm data. Finally, the data are re-gridded to a common coordinate system and a pixel scale of  $10''$ .

#### 4.2. Fitting results

In applying our Bayesian method to the CB244 dataset, we limit our analysis to those pixels containing fluxes in at least each of the five *Herschel* bands, since the SPIRE images have more coverage than the PACS images. In addition, to minimize the impact of uncertainties in the estimated DC-level offset, we limit our analysis to those pixels having  $S/N > 2$  as averaged over the five *Herschel* bands, for which the formal statistical error in the DC-level offset is negligible. The coverage of pixels that we analyze using our hierarchical Bayesian method is shown on the 500  $\mu\text{m}$  map in Figure 5.

We conservatively assume calibration uncertainties of 15% for each of the *Herschel* bands, and calibration uncertainties of 30% and 20% for the 870  $\mu\text{m}$  and 1.3 mm bands, respectively. The values we adopt are larger than the official *Herschel* Science Center (HSC) values, and our reasons are as follows.

For the PACS instrument, the point-source calibration uncertainty is 3% and 5% at 100  $\mu\text{m}$  and 160  $\mu\text{m}$ , respectively. However, we have used versions of the Launhardt et al. (2012, in prep) data reduced with Scanamorphos, a pipeline that is better suited for the analysis of extended emission compared to high-pass filtering. High-pass filtering is another common *Herschel* image analysis technique that removes unknown levels of extended emission and is thus better suited for point-source analysis. We note that the high-pass filtering technique removes  $1/f$  noise more efficiently than other map processing techniques; therefore our Scanamorphos maps may have elevated noise levels by comparison.

Because we are most interested in investigating the ex-

TABLE 2  
ESTIMATED DC-LEVELS, NOISE AMPLITUDES, AND CALIBRATION ERRORS FOR *Herschel* MAPS OF CB244

	100 $\mu$ m	160 $\mu$ m	250 $\mu$ m	350 $\mu$ m	500 $\mu$ m
DC-level <sup>a</sup>	1298	510.0	298.9	169.6	77.19
Noise Amplitude <sup>b</sup>	39.52	75.00	26.54	13.44	7.206
Estimated Calibration Errors <sup>c</sup>	$0.93 \pm 0.14$	$0.90 \pm 0.09$	$1.07 \pm 0.10$	$1.18 \pm 0.14$	$1.26 \pm 0.19$

<sup>a</sup> DC-level in units of  $\mu\text{Jy}/''^2$ , estimated according to the procedure described in § 4.1

<sup>b</sup> Standard deviation in the additive noise in units of  $\mu\text{Jy}/''^2$ , estimated according to the procedure described in § 4.1

<sup>c</sup> The posterior median and standard deviation for the calibration errors. The calibration errors are *a priori* assumed to be log-normally distributed with a geometric mean of unity and an uncertainty of 15%.

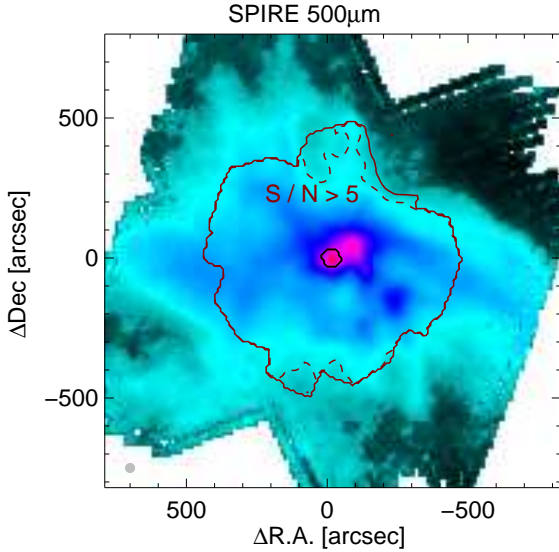


FIG. 5.— Coverage of the CB244 pixels for which we analyzed using our hierarchical Bayesian method, compared with the SPIRE 500  $\mu$ m map. We analyzed pixels that had coverage in all five *Herschel* bands and a mean  $S/N$  over the *Herschel* bands of  $\langle S/N \rangle > 2$ . In addition, we omitted the protostar in the center of the image from our analysis. The grey circle in the lower left corner illustrates the size of the SPIRE 500  $\mu$ m beam.

tended emission, we conclude that reduction techniques that remove extended emission levels, namely high-pass filtering, are not robust for our scientific goals even when they deliver data products with reduced  $1/f$  noise. The main remaining uncertainties are most likely caused by beam convolution effects (e.g., imperfect kernels) and possibly color corrections. These uncertainties are very hard to quantify. Therefore our strategy is to adopt an inflated calibration uncertainty, meant to represent multiple independent source of uncertainty: extended emission calibration uncertainties, the uncertainties introduced by beam convolution,  $1/f$  noise, and other unidentified effects. Thus the final calibration uncertainties we use are 15% and are conservative compared to the HSC recommended point-source calibration uncertainties.

For SPIRE the final HSC recommended calibration uncertainty is 7%. However, the calibration for extended sources is performed by multiplying the calibration for point sources by a correction factor (see Section 5.2.8 of the SPIRE Observers' Manual<sup>6</sup>). No additional extended source calibration uncertainty is discussed to our knowl-

edge, and thus we also assume 15% uncertainty on the calibration for the SPIRE maps. These values are conservative compared to the HSC recommended values for calibration uncertainties.

We employed the color corrections reported in the *Herschel*/SPIRE and *Herschel*/PACS observer's manuals. In general, the color corrections are small. Following Schnee et al. (2010), we ignore the color correction for the  $\lambda = 870 \mu\text{m}$  data, and impose a color correction to the 1.3 mm data by modifying the effective wavelength to be  $\lambda = 1.1 \text{ mm}$ .

Observed fluxes from the centrally-heated protostellar region are affected by line-of-sight temperature variations, and possibly even optically thick dust. Due to these systematic uncertainties, the estimated protostellar values of  $N$ ,  $\beta$ , and  $T$  through Eq. 1 are likely to be highly erroneous, and may even introduce biases into other inferred quantities, such as the mean and covariance of  $\log N(H)$ ,  $\log T$ , and  $\beta$  of the whole sample, as well as the calibration uncertainties. Accordingly, in our analysis we omit the pixels corresponding to the protostar.

We also estimate  $N(H)$ ,  $T$ , and  $\beta$  based on minimizing  $\chi^2$ . Because the  $\chi^2$ -based estimates are unstable at low  $S/N$ , we limit our analysis to those pixels for which the average  $S/N$  over the *Herschel* bands is  $\langle S/N \rangle > 5$ .

The derived relationship between  $\beta$  and temperature for both the Bayesian and  $\chi^2$ -based estimates are shown in Figure 6. The  $\chi^2$ -based estimates suggest a strong anti-correlation between  $\beta$  and  $T$ , as expected. However, the Bayesian analysis finds that  $\beta$  weakly increases as  $T$  increases, which is the opposite trend compared to the  $\chi^2$ -based estimates. The Spearman's rank correlation for the  $\chi^2$ -based estimates is  $\rho = -0.68 \pm 0.01$ , while for the Bayesian estimates it is  $\rho = 0.33 \pm 0.04$ . The correlation between  $\beta$  and  $T$  is rather weak, and while  $\beta$  tends to increase with  $T$  in the mean, there is a large scatter in  $\beta$  at a given temperature.

In Figure 7 we show the SED for the pixel in the prestellar core with highest  $N(H)$ , a pixel with  $\langle S/N \rangle$  similar to the median value, and a pixel with  $\langle S/N \rangle = 5$ . For the prestellar core we find  $T = 11.6 \pm 0.2 \text{ K}$ ,  $\beta = 1.88 \pm 0.13$ , and  $\log N(H) = 22.65 \pm 0.01 \text{ cm}^{-2}$ . For the prestellar core, the  $\chi^2$  estimates are  $T = 10.97 \pm 0.14 \text{ K}$ ,  $\beta = 1.61 \pm 0.05$ , and  $\log N(H) = 22.35 \pm 0.09 \text{ cm}^{-2}$ . The SEDs are compared with the range of greybody models that contain 95% of the posterior probability. In addition, we show the SED derived from the  $\chi^2$  estimates. Note that the Bayesian greybody SED models defined by

<sup>6</sup> [http://herschel.esac.esa.int/Docs/SPIRE/html/spire\\_om.html](http://herschel.esac.esa.int/Docs/SPIRE/html/spire_om.html)

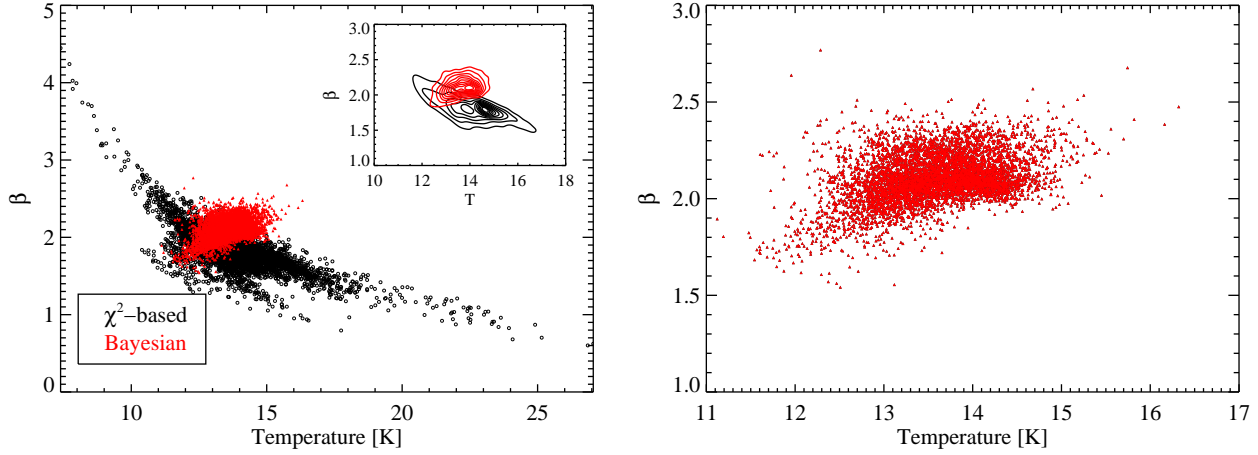


FIG. 6.— The left panel shows the distribution of  $\beta$  and  $T$  for CB244 from minimizing  $\chi^2$  (black open circles) and the random draw from the posterior distribution under our hierarchical Bayesian model (red triangles). The inset provides a close-up of the density of the distribution, while the right panel shows a close-up of the hierarchical Bayesian values. As expected, the  $\chi^2$ -based estimates display an anti-correlation. However, the Bayesian estimates show a weak positive correlation, and there is a large range in  $\beta$  at fixed  $T$ .

the red region do not include the contribution from the calibration uncertainties, and thus it is not appropriate to compare them directly to the data.

In order to assess the quality of fit, we compare the measured fluxes with those predicted by our Bayesian method for each of the three SEDs shown in Figure 7. This is called a “posterior predictive check” (Rubin 1981, 1984; Gelman, Meng, & Stern 1996), and is commonly used to assess the goodness-of-fit of a Bayesian model. For each random draw from our MCMC sampler, we simulate a flux value at each value of  $\nu$ , incorporating the calibration error and measurement noise. Through this process we build up a distribution of predicted fluxes incorporating our uncertainty in the derived parameters. The advantage of this approach is that we compare the actual measured fluxes (which are considered fixed and known) to a distribution of predicted fluxes, instead of simply comparing the measured fluxes at each wavelength to a single best-fit SED. Because the predicted fluxes also have the calibration errors and noise folded in, they are the appropriate quantity to compare to the measured fluxes to test the quality of the fit, and not the model greybody SEDs. Figure 7 also compares the measured fluxes with the ranges containing 95% of the values predicted from our Bayesian approach. In all cases the measured values fall within this range, showing that the Bayesian results are consistent with the measured data, and therefore provide an acceptable fit.

We also checked the derived calibration errors and their uncertainties, in order to ensure that the derived calibrations are consistent with those obtained from the data reduction; i.e., that the calibration errors are consistent with  $\delta_j = 1$ . The estimated calibration errors and their uncertainties are also listed in Table 2. The estimated calibration errors are consistent with unity, implying that we do not find any evidence for significant deviations from the calibrations performed in the data reduction which might be indicative of data systematics or model mis-specification. Moreover, the posterior uncertainties in the derived calibration errors are similar to the *a priori* assumed values of 15%, indicating that essentially all of the information from the calibration errors comes from the prior that we have placed on them. Because of

this, the fact that our method incorporates the calibration errors should not be interpreted as a recalibration of the data. Rather, we have included the calibration errors as nuisance parameters which are identified as an additional source of measurement error. Indeed, it is not the absolute calibration which is included in our statistical model, but rather the error in the calibration. The posterior probability distributions that we obtain from our MCMC method average over the unknown calibration errors, thus ensuring that uncertainties in the calibration are also reflected in the uncertainties in the derived greybody parameters, as well as reflected in the estimated means and correlations (also see the discussion in § 4.3).

As an additional test, we perform cross-validation to compare the hierarchical Bayesian estimates with the  $\chi^2$ -based ones. For this test, we randomly remove 10% of our photometry, and then refit the remaining 90% of the CB244 data. The resulting estimates of  $N(H)$ ,  $\beta$ , and  $T$  were then used to predict the flux values for the 10% of the data that were left out. If the hierarchical Bayesian estimates provide a better description of the SED, then they should do a better job of predicting the data that is omitted from the fit. As a measure of the error in the flux, we use the absolute value of the difference between the measured flux and the model flux, divided by the standard deviation of the noise in that band,  $\sigma_j$ . For our Bayesian estimates, the median of this error is 0.55, while the median for the  $\chi^2$  estimates is 0.90. The hierarchical Bayesian estimates did a factor of  $\sim 2$  better than the  $\chi^2$  estimates in predicting the flux values for data that is omitted from the fit. This result suggests that the Bayesian estimates provide a better description of the SED, and are therefore more reliable than the  $\chi^2$  ones.

The temperature and  $\beta$  maps of CB244 are shown in Figure 8, along with contours of constant column density; all maps were derived from the posterior median values. The temperature tends to decrease toward the center of the prestellar core, while the column density tends to increase toward the center. The  $\beta$ -map illustrates that the values of  $\beta$  trace the column density values very well, with  $\beta$  decreasing toward the central, more dense regions. The estimated  $\beta$  values become noisy near the central dense region of the core, with more drastic spatial vari-



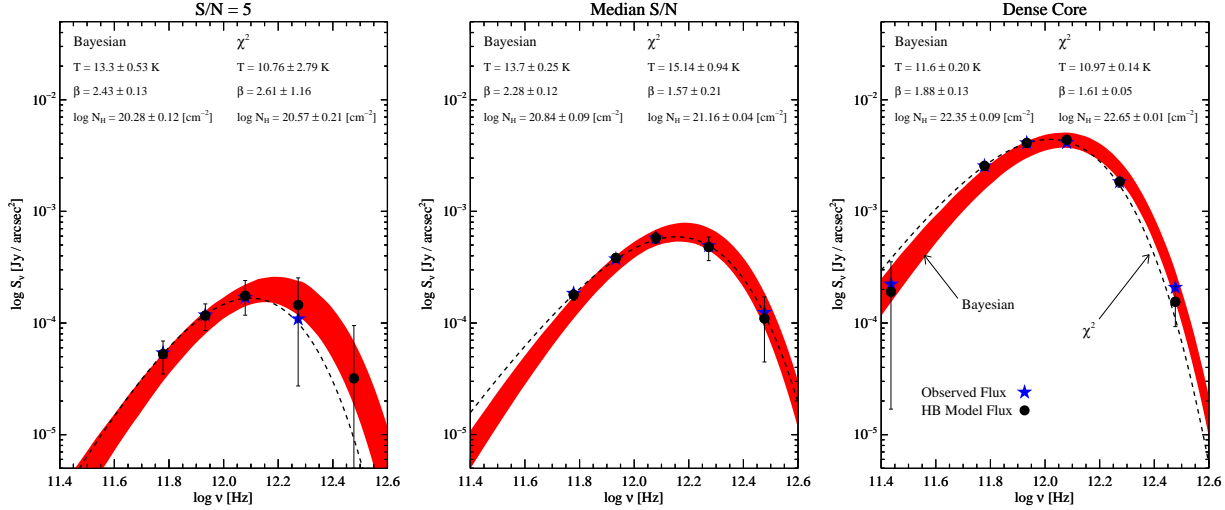


FIG. 7.— Measured fluxes (blue stars) for the pixel with the highest estimated column density in the prestellar core (right), a pixel with average Herschel  $S/N$  similar to the median value (center), and the pixel with average Herschel  $S/N = 5$  (left), which defines the lower limit of our  $S/N$  cut for the  $\chi^2$  estimates. The  $100\mu\text{m}$  flux measurement is missing from the left panel because its value is negative. The best-fit greybody SEDs derived from the  $\chi^2$  estimates are shown with a dashed black line, while the red regions contain 95% of the posterior probability for the greybody SEDs derived from our hierarchical Bayesian method. The measured fluxes are compared with the values that are predicted from our Bayesian model (black circles), with the error bars containing 95% of the posterior probability on the measured SED. The fluxes and their error bars predicted from our Bayesian model differ from the model greybody SEDs in that they also include the effects of the calibration error and noise, and thus it is the green circles that should be compared with the measured data and not the red region. The actual measured values of the flux fall within the range expected from our Bayesian model, and therefore our model is consistent with the measured data.

ations. It is unclear why this is the case, although it may be related to the breakdown of the assumption of optically thin isothermal dust that underpins Equation (1).

Figure 9 shows the distribution of the CB244 data points in the  $N(H)$ – $\beta$  plane, using both the Bayesian and  $\chi^2$ -based estimates. For the Bayesian estimates we show a random draw from the posterior distribution to more faithfully represent the intrinsic scatter in  $\beta$  at a fixed value of  $N(H)$ . As expected from the  $\beta$  map shown in Figure 8, our Bayesian estimates show a tight anti-correlation between column density and  $\beta$ . The anti-correlation between  $\beta$  and  $N(H)$  is also seen with the  $\chi^2$  estimates, but the larger errors in the  $\chi^2$ -based estimates add considerable artificial scatter to the values of  $\beta$  at fixed  $N(H)$ , making the correlation appear less significant. The correlation can be parameterized as

$$\beta = (2.18 \pm 0.18) - (0.27 \pm 0.01) \log \left( \frac{N(H)}{10^{21} \text{ cm}^{-2}} \right). \quad (17)$$

The scatter in  $\beta$  at fixed  $N(H)$  is estimated to have a dispersion of  $\sigma_{\beta|N} = 0.040 \pm 0.003$ . This value of  $\sigma_{\beta|N}$  argues against a constant value of  $\beta$  at fixed column density. The anti-correlation between  $\beta$  and column density is highly significant and is observed even if we limit our analysis to the highest  $S/N$  data.

The  $\beta$  –  $N(H)$  anti-correlation obtained from our Bayesian method is much tighter than that estimated using the  $\chi^2$  estimates. However, we caution that it is unclear if the small scatter in  $\beta$  extends over the entire range in column density probed. Because  $S/N$  is strongly correlated with column density, the pixels with low estimated column density also have low  $S/N$ . For the lower  $S/N$  pixels, the model for the distribution of  $\beta$ ,  $N(H)$ , and  $T$  becomes more informative, and thus the distribution of the low  $N(H)$  estimates strongly depends on ex-

trapolation from the distribution of the high  $N(H)$  estimates. Therefore, the distribution of  $\beta$  at fixed  $N(H)$  at low  $N(H)$  is primarily estimated by extrapolation from the distribution of  $\beta$  at fixed  $N(H)$  at high  $N(H)$ . Our simple Student's  $t$  model fixes the standard deviation of the scatter in  $\beta$  at fixed  $N(H)$  to be constant. Because the scatter in  $\beta$  at fixed  $N(H)$  is small for high  $N(H)$ , where the  $S/N$  is high, the Student's  $t$ -model therefore extrapolates the scatter in  $\beta$  at fixed  $N(H)$  at low  $N(H)$  to also be small.

The increasing influence of extrapolation on our results can be seen more clearly in distribution of  $T$  at fixed  $N(H)$ , where the dispersion in estimated  $T$  at fixed  $N(H)$  increases down to  $N(H) \sim 10^{21} \text{ cm}^{-2}$ , and then becomes constant. This therefore suggests that the estimated values for pixels  $N(H) \lesssim 10^{21} \text{ cm}^{-2}$  are strongly influenced by extrapolation from the pixels with  $N(H) \gtrsim 10^{21} \text{ cm}^{-2}$ . If we had used a more flexible model, such as a mixture of Gaussian functions, then the high  $S/N$  data would not be as informative about the low  $S/N$  data and the scatter in  $\beta$  at fixed  $N(H)$  for the low  $N(H)$  data would be poorly constrained. Because of this, we cannot conclude that the tight anti-correlation derived from our hierarchical Bayesian approach persists across the entire range of column density probed in this analysis, although we do find evidence that it is real at  $N(H) \gtrsim 10^{21} \text{ cm}^{-2}$ . Future work will incorporate more flexible models for the distribution of  $\beta$ ,  $N(H)$ , and  $T$ . However, we also note that the weak positive correlation between  $\beta$  and  $T$  that we observe persists if we limit ourselves to only those pixels with  $N(H) > 10^{21} \text{ cm}^{-2}$ .

Figure 9 also shows the distribution of the CB244 data points in the  $N(H)$ – $T$  plane, using both the Bayesian and  $\chi^2$ -based estimates. As with the  $N(H)$ – $\beta$  distribution, we use a random draw from the posterior distribution for the Bayesian estimates. An anti-correlation between

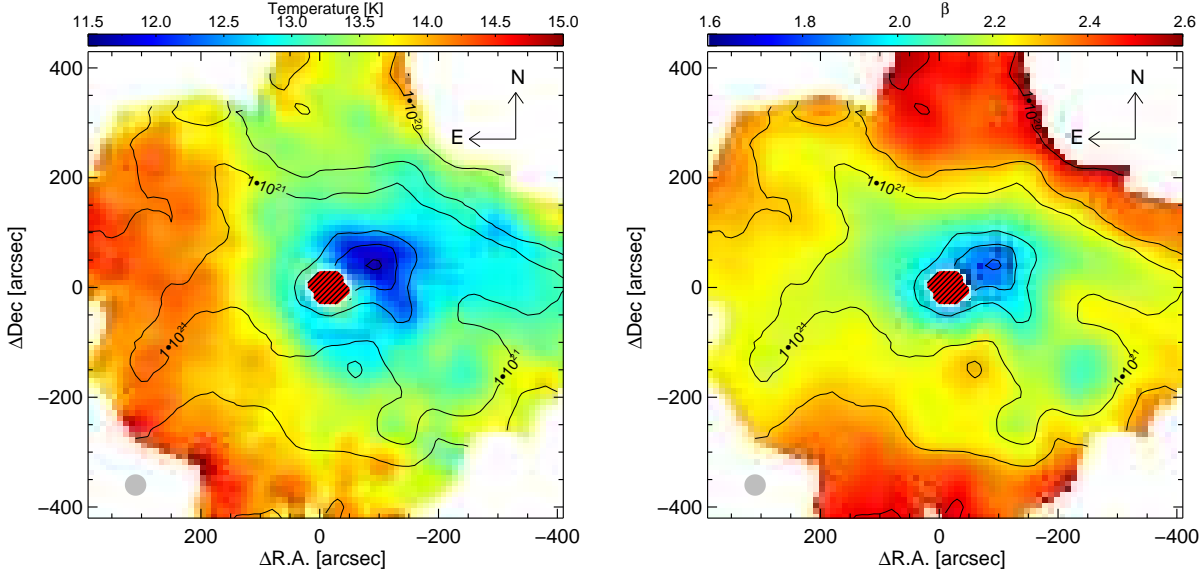


FIG. 8.— Temperature (left) and  $\beta$  (right) map for CB244 derived from the Bayesian estimates. The red hashed region in the center of the images corresponds to the protostar, which we exclude from our analysis, and the grey circle in the lower left corner illustrates the size of the SPIRE 500  $\mu\text{m}$  beam. Overplotted are contours of constant column density, corresponding to  $N(\text{H}) = 10^{20}, 5 \times 10^{20}, 10^{21}, 5 \times 10^{21}, 10^{22}$ , and  $2 \times 10^{22} \text{ cm}^{-2}$ . The coolest and most dense region corresponds to the prestellar core, with the temperature decreasing toward its center. The  $\beta$ -map traces the column density map very well, with the values of  $\beta$  decreasing toward the central, more dense regions.

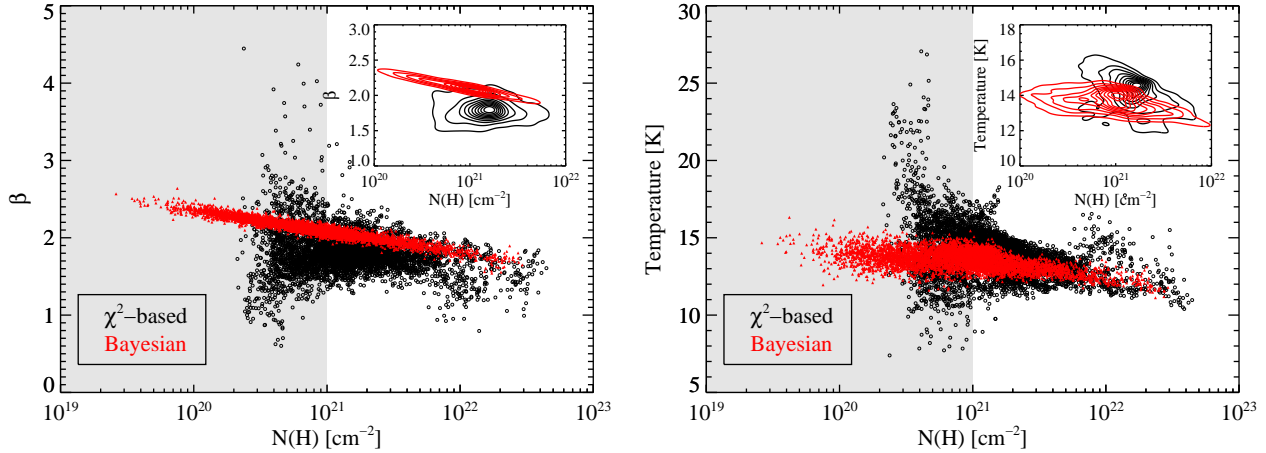


FIG. 9.— Dependence of  $\beta$  (right) and  $T$  (left) on column density,  $N(\text{H})$ . There is a tight and highly significant anti-correlation between column density and  $\beta$ , and there is a weak anti-correlation between column density and temperature. These anti-correlations may be evidence for the growth of dust grains in more dense, cooler environments. In both cases the trends are not as obvious for the  $\chi^2$ -based estimates because large uncertainties artificially broaden the inferred distributions. The estimated values of  $\beta$  and  $T$  based on our Hierarchical Bayesian method likely become strongly influenced by extrapolation from high  $S/N$  data points at  $N(\text{H}) \lesssim 10^{21} \text{ cm}^{-2}$  (shaded region), so we caution that the estimated trends at low  $N(\text{H})$  may not be robust.

column density and temperature is apparent, although it is not as tight as the anti-correlation between  $N(\text{H})$  and  $\beta$ . The anti-correlation between column density and temperature is also manifested in the temperature map of CB244 (Fig. 8), where the temperature decreases toward the central denser regions. However, comparison with the  $\beta$ -map in Figure 8 shows that values of  $\beta \approx 2.2$  are found both in the warmer region to the east of the core, and in the cooler region to the west of the core. These results suggest that density, and not temperature, is the primary driver behind variations in  $\beta$ .

Our analysis also enables us to investigate how  $\beta$  depends on temperature at fixed column density. Although we have found that  $\beta$  and  $T$  are weakly positively correlated in CB244, this is obtained by averaging over the

distribution of  $N(\text{H})$  for CB244. Therefore, it is not necessarily true that  $\beta$  and  $T$  are correlated at fixed  $N(\text{H})$ . We quantify the relationship between  $\beta$  and  $T$  at fixed  $N(\text{H})$  by performing a linear regression of  $\beta$  simultaneously on both  $\log T$  and  $\log N(\text{H})$ , which we derive from our estimated covariance matrix for  $\beta, \log T$ , and  $\log N(\text{H})$ :

$$\beta = (2.29 \pm 0.18) - (0.29 \pm 0.01) \log \left( \frac{N(\text{H})}{10^{21} \text{ cm}^{-2}} \right) - (0.81 \pm 0.19) \log \left( \frac{T}{10 \text{ K}} \right). \quad (18)$$

Interestingly, our results imply that for CB244  $\beta$  and  $T$  are anti-correlated at fixed column density. However,



when averaging over the distribution of column densities  $\beta$  and  $T$  display a weak positive correlation in CB244. The scatter in  $\beta$  at fixed column density and temperature is  $\sigma_{\beta|N,T} = 0.036 \pm 0.002$ , which is only  $\approx 10\%$  smaller than the scatter in  $\beta$  at fixed column density. These results confirm that the variations in  $\beta$  are primarily accounted for by variations in  $N(H)$ , and that temperature is only a minor secondary driver to variations in  $\beta$ .

#### 4.3. Assessing the Impact of Data Systematics

As stated above, we limit our analysis to those pixels with  $\langle S/N \rangle > 2$  over the five *Herschel* bands, with the goal of minimizing the effect of systematic error in the zero-level of the maps, which would affect the faint regions the most. However, it is possible that our results are still affected by systematics regarding the estimated zero-level. Such systematics may result from uncertainties in both the astrophysical and instrumental background levels. In both cases this would result in a spatially-correlated systematic error in all of the flux values across the map. To assess the impact of errors in the estimated zero-level, we perform a few additional checks regarding systematics in the DC-levels. However, we note that in order to fully realize the impact of data systematics on the results for a particular source more rigorous simulations should be performed. As this is beyond the scope of this paper, the tests we perform here are meant to be illustrative of the impact of data systematics on the Hierarchical Bayesian results, and how one might address them in practice. Moreover, we also note that unaccounted systematics also affect the  $\chi^2$ -based results in a similar, if not the same, manner. Thus our result that the Hierarchical Bayesian method leads to opposite conclusions with respect to the  $\chi^2$  estimates regarding the correlations among SED parameters for CB244 is robust against these systematics.

We first assess the impact of systematic uncertainty in the zero-levels of the data from ground based bolometers (i.e., SCUBA and MAMBO). For the ground-based data it is unlikely that the uncertainty in the zero-level is driven by uncertainty in the background emission, as the subtraction of atmospheric emission is taken care of in the measurement procedure. The MAMBO and SCUBA data are chopped at high frequency, and the restored dual beam maps automatically subtract off all atmospheric and astrophysical extended background. The information on the atmospheric emission and extended background are no longer in the data.

In order to assess the robustness of our derived correlations to systematics with respect to the ground-based data, we redid our analysis using only the five *Herschel* maps. Using only the *Herschel* data, the Spearman's rank correlation coefficient for the  $\beta$ - $T$  relationship was  $\rho = 0.37 \pm 0.04$  and the slope of the  $N_H$ - $\beta$  anti-correlation was  $-0.19 \pm 0.01$ . The  $\beta$ - $T$  correlation is essentially unaffected by the removal of the ground-based data, while the  $N_H$ - $\beta$  anti-correlation is reduced in magnitude but still present. Our results are thus qualitatively robust against the zerolevel offsets in data from the groundbased bolometers, which frequently result from the spatial filtering techniques applied during data reduction (e.g., Kauffmann et al. 2008).

As stated earlier, CB244 is part of a larger sample of

Bok globules chosen to lie in relatively isolated regions. These sources were chosen in this manner so as to ensure that they have exceptionally low background emission, and thus uncertainties in the astrophysical background emission should be minimal. The uncertainty in the zero-level for the *Herschel* maps should be driven by the uncertainty in the instrumental background. To assess the impact of mispecifying the zero-levels of the *Herschel* data, we refit the CB244 data using only the *Herschel* bands after adding Gaussian noise to the logarithm of each of the five estimated DC-levels. The standard deviation in the log-normal noise was 5%. This value is much larger than the formal statistical uncertainty on the DC-level as estimated according to the procedure described in § 4.1 (i.e., on the mean value of the best-fit Gaussian function), but it should give us insight into how uncertainty in the DC-level affects the results. Note that each pixel in a map is assumed to have the same DC-level, and thus the perturbed DC-levels introduce the same offset to each of the pixels in a given map.

We did not find any significant difference to the correlations obtained when fitting the maps with the perturbed DC levels; however, there is a large difference in the inferred mean values of  $\beta$  and  $T$ . Using the perturbed data, our MCMC sampler inferred an average value for  $\beta$  and  $T$  of  $\bar{\beta} = -0.26 \pm 0.32$  and  $\bar{T} = 27.3 \pm 0.7$ . This value of  $\bar{\beta}$  is inconsistent with a value of  $\beta \approx 2$  inferred from our CB244 data and from earlier studies. Moreover, for the original CB244 data, the best-fit values of the calibration errors,  $\delta$ , were on average  $0.7\sigma$  away from unity, which is consistent with our prior assumption that the calibration should be correct on average with an uncertainty of  $\approx 15\%$ . However, for the perturbed CB244 data the best-fit values of  $\delta$  were on average  $1.7\sigma$  away from unity. The calibration errors derived from the perturbed data set are inconsistent with our assumption that they on average should equal unity with a dispersion of 15%, correctly suggesting problems with the perturbed data set. The likely reason for this is that the error in the zero-level is partially being absorbed by the estimated values of the calibration errors,  $\delta$ .

As a final test, we fix the calibration errors equal to unity and refit the data using our Hierarchical Bayesian method. This is equivalent to assuming that the calibration is correct and that there is no uncertainty on it. This allows us to test the impact of overestimating the calibration uncertainty, as we have conservatively assumed calibration uncertainties that are larger than the official values recommended by the *Herschel* Science Center. In addition, it allows us a more direct comparison with the  $\chi^2$  results, as the  $\chi^2$  fits ignore the impact of calibration errors. Fixing  $\delta_j = 1$  only resulted in small differences in the estimated mean values and correlations of  $(\log N_H, T, \beta)$ . The derived value of Spearman's rank correlation for the  $\beta$ - $T$  relationship was  $\rho = 0.28 \pm 0.02$  when we ignored the calibration errors, compared to  $\rho = 0.33 \pm 0.04$  obtained when the calibration errors are included. The anti-correlation between  $N_H$  and  $\beta$  is actually stronger when we ignore the calibration errors, having a value of  $\text{Corr}(\log N_H, \beta) = -0.944 \pm 0.004$ , compared to  $\text{Corr}(\log N_H, \beta) = -0.786 \pm 0.040$  obtained when we include the calibration uncertainties.

When we include the calibration errors the derived mean values are  $\langle \log N_H \rangle = 20.90 \pm 0.12$ ,  $\langle \beta \rangle = 1.92 \pm$

0.19, and  $\langle T \rangle = 14.85 \pm 0.42$ . However, when we ignore the calibration errors we find  $\langle \log N_H \rangle = 21.091 \pm 0.006$ ,  $\langle \beta \rangle = 1.797 \pm 0.003$ , and  $\langle T \rangle = 14.153 \pm 0.016$ . Using the median of the  $\chi^2$ -based estimates we find  $\langle \log N_H \rangle = 21.126 \pm 0.005$ ,  $\langle \beta \rangle = 1.787 \pm 0.002$ , and  $\langle T \rangle = 14.265 \pm 0.0179$ . Ignoring the calibration errors produces mean values of the SED parameters and their uncertainties that are similar to those obtained from the  $\chi^2$ -based estimates. In addition, the uncertainties in the means and correlations of the SED parameters are larger when we include the calibration errors, as the calibration uncertainty is reflected in the much larger uncertainties in the SED parameters.

Changing either the DC level or calibration error results in a constant additive or multiplicative offset for each map. While these errors can alter the mean values of the SED parameters, they do not alter their correlations as the correlations are driven by the spatial variations of flux values across the maps, and not by the mean flux value in each map. More complicated spatially-correlated data systematics may produce biases in the inferred correlations among SED parameters. Simulations should be used to assess the impact on the scientific results when strong spatially correlated errors are thought to be present in a data set.

## 5. DISCUSSION

The application of our hierarchical Bayesian method to observed fluxes of CB244 reveals a number of interesting features. First, we find that there is only a limited range in  $\beta$  and  $T$ , with  $\beta \in (1.8, 2.6)$ , and  $T \in (11, 16)$  K. Second,  $\beta$  and  $T$  are positively correlated, albeit weakly so, suggesting that the strong anti-correlation seen in previous work is driven by noise. Further, the Bayesian fit suggests that  $\beta$  declines towards the central region of the starless core, where the temperature decreases and the column density increases (Fig. 8). In fact, the parameterization of  $\beta$  in terms of  $N$  and  $T$  in Equation 18 indicates that  $\beta$  is more strongly correlated with  $N$  than on  $T$ .

While we have found a number of interesting features in our analysis of CB244, their interpretation is more difficult. Strictly speaking, our derived trends are with respect to the isothermal greybody SED parameters, which are not necessarily equivalent to the corresponding physical parameters that they are intended to estimate. Thus, it is unclear if our derived correlations represent astrophysically-meaningful correlations, or are instead driven by systematics involving the data reduction, background subtraction, and SED model. Such trends may be driven by variations in temperature and density along the line-of-sight, which are currently not accounted for in our analysis. For example, the apparent correlation between  $\beta$  and  $N_H$  cannot be the actual physical correlation as there is both low and high-density gas along the line of sight. The physical cause could be a correlation between volume density and  $\beta$ . In this sense it is also possible that such trends are at least in part driven by real astrophysical variations, possibly due to the growth of dust grains. In high density compressed regions of the ISM, grain sizes may increase due to dust coagulation, possibly leading to an increase in  $\beta$ . Compared to the ISM values of  $\beta \sim 2$ , lower  $\beta \lesssim 1$  are found in numerous studies of protoplanetary disks (e.g.

Miyake & Nakagawa 1993; Mannings & Emerson 1994; Draine 2006; Ricci et al. 2011). The interpretation is that grains in disks are much larger than in the more diffuse ISM, and that these grains are the seeds of protoplanets. The difference in grain sizes between the large scale ISM and protoplanetary disks suggests that during some epoch of the star formation process, grains begin to grow. While this is an intriguing interpretation of our results we stress that we are currently not in a position to sort out the contributions to our inferred correlation from the systematics and real astrophysical variations; future work will address systematic errors resulting from our assumptions of optically-thin isothermal dust.

In order to accurately map the  $T$ ,  $\beta$ , or density structure of an observed region, line-of-sight variations must be taken into account. For example, Shetty et al. (2009b) find that when the model  $\beta$  is constant but there are temperature variations along the line-of-sight, the assumption of isothermality produces  $\beta$  estimates which are inversely correlated to the fitted temperatures. Line-of-sight  $T$  variations will effect both the hierarchical Bayesian and  $\chi^2$  fits of Equation (1) to the observed fluxes in the same manner. This is because the Bayesian and  $\chi^2$  estimates become equivalent in the limit of infinite  $S/N$ . Because our hierarchical Bayesian model accounts for the statistical errors, the results obtained from it should be interpreted as an estimate of what would have been obtained if there is no measurement error. It may be that the relationships that we find between  $\beta$ ,  $T$ , and  $N(H)$  are driven at least in part by line-of-sight variations, making their astrophysical interpretation difficult.

In addition to biases due to line-of-sight variations, our hierarchical Bayesian results may be biased by the optically-thin approximation to the SED. We can estimate the magnitude of this bias using the results from the cross-validation test, described in § 4.2. Because the 100  $\mu\text{m}$  map should be the most affected by the optically-thin approximation, if the optically-thin approximation is not valid we might expect the error in the 100  $\mu\text{m}$  data that was omitted from the fit to be systematically under- or overestimated. We did not notice any significant offset in the cross-validation error for either the  $\chi^2$  or hierarchical Bayesian estimates. Moreover, under our assumption of  $\kappa_0 = 0.009 \text{ cm}^2/\text{g}$  with  $\nu_0 = 230 \text{ GHz}$ , we estimate the optical depth at 100  $\mu\text{m}$  in the core to be  $\tau \approx 0.05$ . Therefore we do not find any significant evidence that the optically-thin approximation is having a strong affect on our results.

We can be confident that statistical uncertainties which lead to spurious and pronounced  $T - \beta$  anticorrelations are appropriately handled in the hierarchical Bayesian method, and thus our inferred correlations are statistically significant. However, systematic errors due to mispecification of the SED model, such as line-of-sight variations, also affect our hierarchical Bayesian results. There may also be difficulties with the data reduction that can introduce spatially-correlated systematic errors, such as unidentified background emission from astrophysical sources, which in turn can bias the inferred correlations. Therefore at this time we cannot disentangle systematic effects from real physical effects in our inferred correlations. Nevertheless, because the hierarchical Bayesian fits rigorously and correctly account for

the statistical errors, we are now in a position to isolate the effects of systematic errors on the scientific conclusions. A thorough analysis of possible approaches to account for line-of-sight variations which does not rely on the optically-thin approximation will be investigated in a future publication. We will also apply our method to a large sample of starless cores in order to investigate if the trends derived here for CB244 extend to a larger sample, providing a more thorough treatment of data systematics.

## 6. SUMMARY

We have developed a hierarchical Bayesian method that rigorously treats measurement errors for fitting single-temperature greybody SEDs. The Bayesian method provides a probability distribution for the values of temperature  $T$ , spectral index  $\beta$ , and column density  $N$  in each pixel (or source), conditional on the measured data, as well as for the distribution of these parameters over an entire map (for a resolved source) or survey (for multiple unresolved sources). In testing the hierarchical Bayesian method on model sources, we demonstrate that it can accurately recover the true parameters and correlations, whereas the  $\chi^2$  fit produces an artificial  $T - \beta$  anti-correlation due to the degeneracy between  $T$  and  $\beta$ .

We have applied our hierarchical Bayesian model to *Herschel* and ground-based observations of the Bok globule CB244. The Bayesian fit estimates  $\beta \in (1.8, 2.6)$ ,  $T \in (11, 16)$  K, which is significantly more constrained than the  $\chi^2$  estimates. Further, we find that  $\beta$  and  $T$  are weakly positively correlated, in direct opposition to the  $\chi^2$  results. We have mapped out the spatial distribution of  $T$ ,  $\beta$ , and  $N_H$ , and the correlations between these properties. We find that  $\beta$  decreases from  $\sim 2.6$  where  $N_H \sim 3 \times 10^{19} \text{ cm}^{-2}$ , to  $\sim 1.8$  in the densest region of the starless core, where  $N_H \gtrsim 10^{22} \text{ cm}^{-2}$ . While

these results may be at least partially driven by systematics regarding the data reduction and the modeling, our method properly corrects for the statistical uncertainties, illustrating that the  $\chi^2$  results are significantly affected by noise.

Due to the accuracy of the hierarchical Bayesian method, and its estimate of a positive correlation between  $T$  and  $\beta$ , it may be used to assess any  $T - \beta$  anti-correlation found from  $\chi^2$  fits. Our analysis demonstrates that hierarchical Bayesian methods can accurately estimate the dependence between SED parameters, and therefore may be used to further understand grain evolution in the ISM.

## ACKNOWLEDGEMENTS

We are grateful to Scott Schnee, David Hogg, Karin Sandstrom, Cornelis Dullemond, Chris Beaumont, Paul Clark, Ralf Klessen, Bruce Draine, Jonathan Foster, Xiao-Li Meng, Alexander Blocker, and Chris Hayward for useful discussions regarding dust emission and Bayesian inference. We are also grateful to an anonymous referee whose suggestions for additional tests helped improve the paper. This material is based upon work supported by the National Science Foundation under Grant No. AST-0908159. BK acknowledges support by NASA through Hubble Fellowship grants #HF-01220.01 and #HF-51243.01 awarded by the Space Telescope Science Institute, which is operated by the Association of Universities for Research in Astronomy, Inc., for NASA, under contract NAS 5-26555, and from the Southern California Center for Galaxy Evolution, a multi-campus research program funded by the University of California Office of Research. RS is supported by the German Bundesministerium für Bildung und Forschung via the ASTRONET project STAR FORMAT (grant 05A09VHA), and the SFB 881 “The Milky Way System.”

## REFERENCES

- Adams F. C., Lada C. J., Shu F. H., 1987, *ApJ*, 312, 788  
Agladze, N. I., Sievers, A. J., Jones, S. A., Burlitch, J. M., & Beckwith, S. V. W. 1996, *ApJ*, 462, 1026  
Anderson L. D., Zavagno A., Rodón J. A., Russeil D., Abergel A., Ade P., André P., Arab H., Baluteau J., Bernard J., Blagrove K., Bontemps S., et al. 2010, *A&A*, 518, L99+  
Aniano, G., Draine, B. T., Gordon, K. D., & Sandstrom, K. 2011, *PASP*, 123, 1218  
Barnard, J., McCulloch, R., & Meng, X-L. 2000, *Statistica Sinica*, 10, 1281  
Beuther H., Henning T., Linz H., Krause O., Nielbock M., Steinacker J., 2010, *A&A*, 518, L78+  
Blain A. W., Barnard V. E., Chapman S. C., 2003, *MNRAS*, 338, 733  
Boudet, N., Mutschke, H., Nayral, C., Jäger, C., Bernard, J.-P., Henning, T., & Meny, C. 2005, *ApJ*, 633, 272  
Carroll, R. J., Ruppert, D., Stefanski, L. A., Crainiceanu, C. M., 2006, *Measurement Error in Nonlinear Models: A Modern Perspective* (2nd ed.; Boca Raton:Chapman & Hall/CRC)  
Evans, N. J., II, Rawlings, J. M. C., Shirley, Y. L., & Mundy, L. G. 2001, *ApJ*, 557, 193  
Draine, B. T. 2006, *ApJ*, 636, 1114  
Draine B. T., Lee H. M., 1984, *ApJ*, 285, 89  
Dupac X., Bernard J.-P., Boudet N., Giard M., Lamarre J.-M., Mény C., Pajot F., Ristorcelli I., Serra G., Stepnik B., Torre J.-P., 2003, *A&A*, 404, L11  
Gelman, A., Carlin, J. B., Stern, H. S., & Rubin, D. B. 2004, *Bayesian Data Analysis* (2nd ed.; Boca Raton:Chapman & Hall/CRC)  
Gelman, A., & Hill, J. 2007, *Data Analysis Using Regression and Multilevel/Hierarchical Models* (New York:Cambridge University Press)  
Gelman, A., Meng, X. L., & Stern, H. S. 1998, *Statistica Sinica*, 6, 733  
Goldsmith, P. F., Bergin, E. A., & Lis, D. C. 1997, *ApJ*, 491, 615  
Griffin, M. J., et al. 2010, *A&A*, 518, L3  
Hayward, C. C., Kereš, D., Jonsson, P., et al. 2011, *ApJ*, 743, 159  
Henning T., Linz H., Krause O., Ragan S., Beuther H., Launhardt R., Nielbock M., Vasyunina T., 2010, *A&A*, 518, L95+  
Hildebrand, R. H. 1983, *QJRAS*, 24, 267  
Hogg, D. W., Myers, A. D., & Bovy, J. 2010, *ApJ*, 725, 2166  
Juvela, M., et al. 2011, *A&A*, 527, A111  
Keene J., Hildebrand R. H., Whitcomb S. E., Harper D. A., 1980, *ApJL*, 240, L43  
Loredo, T. J. 2004, *American Institute of Physics Conference Series*, 735, 195  
Kauffmann, J., Bertoldi, F., Bourke, T. L., Evans, N. J., II, & Lee, C. W. 2008, *A&A*, 487, 993  
Kelly, B. C. 2007, *ApJ*, 665, 1489  
Kelly, B. C., 2011, *J. Comput. & Graph. Stat.*, 20, 584  
Lagache G., Puget J., Dole H., 2005, *ARA&A*, 43, 727  
Launhardt R., Nutter D., Ward-Thompson D., Bourke T. L., Henning T., Khazadyan T., Schmalzl M., Wolf S., Zylka R., 2010, *ApJS*, 188, 139  
Linz H., Krause O., Beuther H., Henning T., Klein R., Nielbock M., Stecklum B., Steinacker J., Stutz A., 2010, *A&A*, 518, L123+

- Mandel, K. S., Narayan, G., & Kirshner, R. P. 2011, *ApJ*, 731, 120
- Miyake, K., & Nakagawa, Y. 1993, *Icarus*, 106, 20
- Malinen, J., Juvela, M., Collins, D. C., Lunttila, T., & Padoan, P. 2011, *A&A*, 530, A101
- Mannings, V., & Emerson, J. P. 1994, *MNRAS*, 267, 361
- Ossenkopf, V., & Henning, T. 1994, *A&A*, 291, 943
- Paradis D., Veneziani M., Noriega-Crespo A., Paladini R., Piacentini F., Bernard J. P., de Bernardis P., Calzoletti L., Faustini F., Martin P., Masi S., Montier L., et al. 2010, *A&A*, 520, L8+
- Pilbratt G. L., Riedinger J. R., Passvogel T., Crone G., Doyle D., Gageur U., Heras A. M., Jewell C., Metcalfe L., Ott S., Schmidt M., 2010, *A&A*, 518, L1+
- Planck Collaboration Ade P. A. R., Aghanim N., Arnaud M., Ashdown M., Aumont J., Baccigalupi C., Balbi A., Banday A. J., Barreiro R. B., et al. 2011, (arXiv:1101.2035)
- Poglitsch, A., et al. 2010, *A&A*, 518, L2
- Ricci, L., Mann, R. K., Testi, L., Williams, J. P., Isella, A., Robberto, M., Natta, A., & Brooks, K. J. 2011, *A&A*, 525, A81
- Rubin, D. B. 1981, *J. Educational Statistics*, 6, 377
- Rubin, D. B. 1984, *Annals of Statistics*, 12, 1151
- Sajina A., Scott D., Dennefeld M., Dole H., Lacy M., Lagache G., 2006, *MNRAS*, 369, 939
- Schnee S., Enoch M., Noriega-Crespo A., Sayers J., Terebey S., Caselli P., Foster J., Goodman A., Kauffmann J., Padgett D., Rebull L., Sargent A., Shetty R., 2010, *ApJ*, 708, 127
- Shetty R., Kauffmann J., Schnee S., Goodman A. A., 2009a, *ApJ*, 696, 676
- Shetty R., Kauffmann J., Schnee S., Goodman A. A., Ercolano B., 2009b, *ApJ*, 696, 2234
- Stutz A., Launhardt R., Linz H., Krause O., Henning T., Kainulainen J., Nielbock M., Steinacker J., André P., 2010, *A&A*, 518, L87+
- Stutz, A. M., Rieke, G. H., Bieging, J. H., et al. 2009, *ApJ*, 707, 137
- Watson A. M., Stapelfeldt K. R., Wood K., Ménard F., 2007, *Protostars and Planets V*, pp 523–538
- Yang M., Phillips T., 2007, *ApJ*, 662, 284
- Yu, Y., & Meng, X-L. 2011, *J. of Comput. & Graph. Stat. (with discussion)*, 20, 531